Liquid-liquid phase separation of tau driven by hydrophobic interaction facilitates fibrillization of tau

Yanxian Lin[1],*, Yann Fichou[2],*, Andrew P. Longhini[3], Luana C. Llanes[2,4], Yinson Yin[2], Guillermo C. Bazan[5], Kenneth S. Kosik[3,6], Songi Han[2,7]†

[1] Biomolecular Science and Engineering, University of California, Santa Barbara, CA 93106

[2] Department of Chemistry and Biochemistry, University of California, Santa Barbara, CA 93106

[3] Molecular, Cell and Developmental Biology, University of California, Santa Barbara, CA 93106

[4] Center for Polymers and Organic Solids, University of California, Santa Barbara, CA 93106

[5] Departments of Chemistry and Chemical Engineering, National University of Singapore, 117543 Singapore

[6] Neuroscience Research Institute, University of California, Santa Barbara, CA 93106

[7] Department of Chemical Engineering, University of California, Santa Barbara, CA 93106

* equal contributions.

† corresponding author: Songi Han. Email: songihan@ucsb.edu

Abstract

Amyloid aggregation of tau protein is implicated in neurodegenerative diseases, yet its facilitating factors are poorly understood. Recently, tau has been shown to undergo liquid liquid phase separation (LLPS) both *in vivo* and *in vitro*. LLPS was shown to facilitate tau amyloid aggregation in certain cases, while independent of aggregation in other cases. It is therefore important to understand the differentiating properties that resolve this apparent conflict. We report on a model system of hydrophobically driven LLPS induced by high salt concentration (LLPS-HS), and compare it to electrostatically driven LLPS represented by tau-RNA/heparin complex coacervation (LLPS-ED). We show that LLPS-HS promotes tau protein dehydration, undergoes maturation and directly leads to canonical tau fibrils, while LLPS-ED is reversible, remains hydrated and does not promote amyloid aggregation. We show that the nature of the interaction driving tau condensation is the differentiating factor between aggregation-prone and aggregation-independent LLPS.

Introduction

Tau is a protein mainly present in the central nervous system that binds and stabilizes microtubules in neurons [1]–[3]. Under healthy conditions, tau is soluble across a wide range of temperatures, protein concentrations, pH and ionic strengths of the buffer, while under pathologic conditions, tau undergoes amyloid aggregation that yields insoluble, irreversible and cross-β rich fibrils. While the functions of tau are not fully understood, in the healthy state tau is tightly bound to microtubules [4] and the concentration of the unbound tau protein is exceptionally low—on the order of 1~10 nM [1]. Under pathological conditions, intracellular tau transforms from its microtubule-bound or soluble state to a fibrillar state. In fact, intracellular deposits of aggregated

---

[1] Estimated from tubulin concentration of 40 μM [5], total tau concentration (bound and free) of 1 ~ 2 μM [6], dissociation constant of 0.1 ~ 1 μM [4] as well as stoichiometry of ~0.5 tau/tubulin dimer [7]. See Materials and Methods for calculation.

42 tau are a diagnostic hallmark of a wide range of neurodegenerative diseases known as tauopathies

43 [8]. The mechanism by which low concentrations of tau is recruited to assemble into tangles

44 remains undetermined. Hence, factors that drive assembly and condensation, or generally

45 mechanisms that increase the intracellular local concentration of tau are of great interest to

46 understand this important pathological process.

47   Liquid-liquid phase separation (LLPS) is a process that is readily driven by multivalent

48 weak interactions between flexible polymers, yielding a polymer-rich phase separated from a

49 polymer-depleted phase [9], [10], the former of which is usually observed as micrometer size

50 fluidic droplets. Here, we use the widest definition of polymers that hence includes intrinsically

51 disordered proteins (IDPs) and ribonucleic acid (RNA). LLPS has been used to describe the

52 formation of membraneless organelles *in vivo* that are proposed to play important roles in

53 mediating cellular functions [11], [12]. The interest in biomolecular condensates in the cellular

54 context has exploded in recent years, fueled by intriguing observations of LLPS of IDPs associated

55 with neurodegenerative diseases, including FUS, TDP-43, hnRNPA1, synuclein [13]–[18] as well

56 as more recently tau [19]–[25]. Despite the ubiquitous occurrence of LLPS with IDPs, the physical

57 principles that govern their formation, phase diagrams or properties are not universal. LLPS of

58 IDPs can be driven by a variety of interaction types and with a wide range of interaction strengths.

59 The driving interaction for association that forms the basis for LLPS typically includes electrostatic

60 charge-charge and dipole-dipole interactions between the backbone, charged/polar side chains and

61 polar solvent molecules, and hydrophobic interactions. The latter involve water-repelling protein

62 or polymer side chains that can be aromatic [26], non-polar [9], [27] or even charged residues [28],

63 [29] that, in the context of the protein or polymer surface, may display less favorable protein-water

64 interactions compared to protein-protein and water-water interactions. Molecular crowding, often

65 modeled by adding polyethylene glycol (PEG), can therefore enhance hydrophobic interactions by

66 removing hydration water from the dense LLPS phase [30]. However, the potentially differential

67 role of electrostatic and hydrophobic interactions for the LLPS of tau have neither been

68 investigated nor dissected to date. Recent work [9], [26], [31]–[35] has highlighted certain

69 interactions as particularly important in driving protein LLPS, in particular π-π and π-cation

70 interaction between charged and aromatic residues [36], [37]. Tau has few aromatic amino acids

71 (~2% for full length tau 2N4R) or arginine residues (~3% for 2N4R), consequently little possibility

72 to engage in π-π or π-cation interactions. Nevertheless, tau's sequence exhibits a rich landscape of

73   chemical properties with polar, charged and hydrophobic residues present throughout the protein.

74   There is a need to study the driving forces of tau LLPS and uncover what role they play in

75   pathology.

76   LLPS has been shown to promote amyloid aggregation of FUS and hnRNPA1 [13]–[16].

77   The verdict is not so clear for LLPS of tau. Ambadipudi *et al.* in 2017 [19] and Wegmann *et al.* in

78   2018 [20] proposed that tau in a LLPS state actively promoted amyloid aggregation, while a recent

79   study from our group [38] showed that tau in LLPS formed by complex coacervation with RNA

80   does not induce or protect from aggregation. Herein, we extensively explore the hypothesis that

81   the nature of the interactions driving tau LLPS is the main factor that influence how LLPS impact

82   amyloid aggregation.

83   We and others have previously shown that tau undergoes electrostatically driven LLPS

84   (LLPS-ED), either with itself—in a process known as simple coacervation (SC)—or with

85   polyanions—in a process known as complex coacervation (CC) [21], [22], [33], [38]. Meanwhile,

86   tau can undergo LLPS upon addition of high concentration of salt (LLPS-HS)[38]. Concentrated

87   salt (e.g. of NH_{4+}, K_+ or Na_+ along the Hofmeister series) has been shown to exert a "salting-out"

88   effect [39], [40], presumably by dehydrating the protein and promoting entropy-driven

89   hydrophobic interactions among proteins [41], [42]. High concentration of salt including NaCl has

90   been found to induce LLPS of several proteins, including BSA [43], lysozyme [44] and most

91   recently FUS, TDP-43, and Annexin A11 [45]. In this article, we use the condensation of tau

92   induced by adding high concentration of salt (LLPS-HS) as a model for tau LLPS driven by

93   hydrophobic interactions. Using EPR spectroscopy, fluorescence spectroscopy and biochemical

94   assays, we compared the properties of tau in LLPS-HS with that of LLPS-ED formed by tau-tau

95   or tau-RNA to uncover whether there is a cause-effect relationship between the LLPS and

96   aggregation of tau.

97

RESULTS

99   **Tau undergoes LLPS at high salt concentration**

100

101   The longest human tau isoform (2N4R) is a charged and hydrophilic IDP near physiological

102   conditions, displaying both high solubility and stability. The charge and Hopp-Woods

103 hydrophobicity plots (both are moving-averaged over 25 consecutive residues) show that 2N4R
104 consists of a hydrophilic and negatively charged N-terminal half and a weakly hydrophobic and
105 overall positively charged C-terminal half (**Figure 1**A). The four repeat domains (R1–R4) are
106 responsible for binding microtubules and constitute a large part of the core of amyloid fibrils found
107 *in vivo* and *in vitro* [46]. The goal of our study is to investigate tau LLPS based on hydrophobic
108 interactions separately from those based on electrostatic interactions. To maximize the
109 hydrophobicity while keeping the repeat domains, we studied the LLPS of N-terminal-truncated
110 2N4R between residues 255-441, referred to as tau187 (**Figure 1**A). To mute potential effects of
111 covalent disulfide bonding, we introduced double site mutations to the two native cysteines,
112 C291S/C322S. Unless stated explicitly, we refer to tau187C291SC322S as tau187, and to
113 2N4RC291SC322S as 2N4R throughout this work.

114   To eliminate electrostatic interactions, we mixed tau with excess amount of NaCl. Both
115 tau187 and 2N4R samples became turbid and formed abundant droplets when [NaCl] was adjusted
116 to above 4 M and 4.75 M, respectively (**Figure 1**B). After formation, droplets merged within
117 seconds, confirming their fluidity (**Figure 1**C). We refer to this process of high salt concentration-
118 induced LLPS as LLPS-HS, and the resulting droplets as high salt droplets in this article. We
119 furthermore confirmed that both tau187C291S and tau187C291SP301L form LLPS-HS (Figure 1-
120 figure supplement 1), showing that inter-tau disulfide bonding and aggregation-prone mutations
121 do not prevent LLPS-HS.

122   We have previously shown that tau187 undergoes LLPS-ED, and established a phase
123 diagram using a combination of experiments, theory underlying coacervation and field theoretic
124 simulations (FTS) of LLPS [22]. The LLPS-ED phase (formed either by SC or CC) typically
125 dissolves at a total salt concentration above [NaCl] ~ 100-200 mM [22], [33], while the LLPS-HS
126 obviously only forms above a much higher salt concentration (3-4 M; **Figure 1**B). The question
127 we ask is whether the properties of the protein tau and the LLPS phase are different between the
128 two forms of LLPS. We start by testing the sensitivity of the dense liquid phase to 1,6-hexanediol
129 (1,6-HD), an amphiphilic small molecule that is known to disrupt weak hydrophobic interactions,
130 [47]–[49] which has been widely used to verify the formation and dissolution of various forms of
131 LLPS, including that of FUS [50] and of tau [20], [51]. We prepared tau LLPS-ED in two ways:
132 by mixing tau187 with RNA by the CC mechanism, or by lowering the ionic strength of the
133 solution containing 2N4R (< 10 mM, referred to as low-salt droplets) that induces SC (**Figure 1**D).

134   When adding 4% 1,6-HD, neither form of tau LLPS-ED, tau-RNA droplets formed by CC or tau

135   low-salt droplets formed by SC, dissolved. In contrast, tau LLPS-HS dissolved completely upon

136   addition of 4% 1,6-HD (**Figure 1**D).

137   The distinct effect of 1,6-HD demonstrates that the tau molecules are held together in the

138   condensed phase of LLPS by different types of interactions in LLPS-ED versus in LLPS-HS. The

139   observation that the stability of LLPS-ED, whether formed of tau187-RNA CC or of 2N4R SC, is

140   insensitive to 1,6-HD confirmed that the interactions holding tau together in the condensed phase

141   is not weakened by an amphiphilic molecule; this behavior is expected for purely electrostatic

142   associations. Considering that the Debye length at 4 M NaCl is ~0.1 nm, which is much smaller

143   than the diameter of a water molecule [52], [53], electrostatic interactions between tau molecules

144   are muted in LLPS-HS. Besides electrostatic screening, salts made of Na_+ and Cl_- at these

145   concentrations also exert dehydration induced salting out of proteins following the Hofmeister

146   series. Together with the observation that 1,6-HD dissolves high salt droplets, these results

147   demonstrate that LLPS-HS are predominantly hydrophobically driven. Hydrophobic interactions

148   arise from weaker protein-water compared to water-water and protein-protein interactions,

149   resulting in (i) water to be readily expelled from the protein surface to rather hydrogen bond with

150   other solvent molecules, i.e. other water molecules in the bulk, and (ii) protein molecules to interact

151   via van der Waals interactions. Amphiphilic molecules such as 1,6-HD can restore interactions

152   between protein and water and/or disrupt interaction between associated proteins, disrupting the

153   hydrophobic driving forces for LLPS-HS. These results verify that LLPS-HS is a good model

154   system to study the consequences of hydrophobically driven LLPS on the irreversible process of

155   aggregation.

156

157   **LLPS-HS undergoes irreversible maturation.**

158

159   Many examples of protein LLPS have been shown to undergo irreversible maturation [16], [54].

160   To study the reversibility property of LLPS-HS, we recorded turbidity of high salt droplet samples

161   upon repeated heating-cooling cycles. At 3.5 M NaCl, turbidity at T < 35 ℃ remains near zero and

162   significantly increases to 0.4 at T > 40 ℃, indicating a lower critical saturation temperature

163   behavior (LCST) where LLPS is thermodynamically more favorable at higher temperature (**Figure

164   2-figure supplement 1**A). When cooled down to low temperature, the original transparent sample

165   remained slightly turbid (**Figure 2-figure supplement 1**A), a second heating-cooling cycle

166 showed further increase of remaining turbidity. In contrast, tau-RNA LLPS-ED formed by CC

167 showed no remaining turbidity after consecutive heating-cooling cycles (**Figure 2-figure**

168 **supplement 1**B). The same results were found with 2N4R (**Figure 2-figure supplement 1**C). The

169 hysteresis in the build-up of turbidity with repeated heating-cooling cycle implies that LLPS-HS

170 leads to partially irreversible associations between tau, while LLPS-ED formation and melting is

171 reversible.

172 To further probe the micro-environment inside droplets, we labeled tau with an in-house

173 synthesized fluorescence molecular rotor derived from a boron-dipyrromethene (BODIPY) core

174 [55] and performed Fluorescence Lifetime Image Measurements (FLIM) over the course of 48

175 hours (See Materials and Methods for synthesis and microscopy details). Molecular rotors are a

176 class of dyes whose fluorescent lifetimes are sensitive to the local microviscosity of their

177 environment, with a low lifetime indicating a fluid, water-like environment and a high lifetime

178 representing a viscous environment [56]–[58]. Further, within a limited regime, the relationship

179 between the fluorescent lifetime and the microviscosity follows the Förster-Hoffman equation (see

180 calibration between fluorescent lifetime and viscosity in **Figure 2-figure supplement 2**). Unlike

181 viscosity that describes the bulk property of a liquid, microviscosity describes the friction that, in

182 this case, is experienced by a single biomolecule due to its local environment. The molecular rotor

183 was conjugated to 2N4R, as described in Materials and Methods. FLIM images were collected on

184 a confocal microscope and a pixelwise fit of the images binned into histograms. Shortly after

185 triggering LLPS, 2N4R LLPS-HS droplets showed a Gaussian distribution of lifetimes centered

186 around 4.08±0.32 ns (916 cP). In comparison, 2N4R LLPS-ED droplets formed by CC between

187 2N4R and RNA (**Figure 2**E, F) showed a lifetime centered around 3.55±0.07 ns (195 cP). In other

188 words, 2N4R in LLPS-HS experiences a higher microviscosity than in LLPS-ED. After a 48 hour

189 incubation period, the average fluorescence lifetime of 2N4R in LLPS-HS samples increased from

190 4.08±0.26 to 4.15±0.13 ns (**Figure 2**F), while that of 2N4R in LLPS-ED decreased from 3.55±0.07

191 ns to 3.39±0.12 ns (**Figure 2**E, F). Concurrently, amorphous, non-spherical condensates formed

192 within LLPS-HS, while the overall droplet shape of LLPS-ED (of 2N4R-RNA CC) remains

193 spherical (**Figure 2**B, D). The emergence of non-spherical structures within the droplets and the

194 increase in microviscosity sensed by the tau protein indicate that LLPS-HS undergo maturation of

195 the condensate. LLPS-ED on the other hand retains liquid properties that appears to slightly less

196 viscous over time.

197

LLPS-HS triggers canonical tau amyloid aggregation

199

200 To test the hypothesis that maturation of droplets is associated with amyloid formation in the

201 sample, we incubated high salt droplets with a trace amount of Thioflavin T (ThT). While high

202 salt droplets emerge spontaneously and fully upon preparing samples under droplet-forming

203 conditions, ThT fluorescence starts from baseline and steadily increases over ~24 hour duration

204 (**Figure 3**A). The increase of ThT fluorescence reflects an increase in cross-β sheet content

205 developing over hours. Subsequent imaging of tau samples—in LLPS-HS conditions after

206 overnight incubation— showed fibril-like species by TEM that are visually similar to tau-heparin

207 fibrils (**Figure 3**B). This supported the hypothesis that LLPS-HS is followed by the amyloid

208 aggregation of tau.

209 To show the connection between LLPS-HS and amyloid aggregation, we incubated tau at

210 equal concentration, while varying [NaCl] on a multi-well plate. We recorded bright field

211 microscope images before incubation showing the amount of high salt droplets, after which we

212 monitored ThT fluorescence over time (**Figure 3**A). The abundance of droplets visually observed

213 via bright field microscope imaging immediately after sample preparation (at $t = 0$) strongly

214 correlates with the ThT fluorescence intensity after incubation ($t = 24$ hours). The same results

215 were found with 2N4R (**Figure 3-figure supplement 2**). The initial turbidity (at 500 nm) that

216 quantifies the volume fraction of high salt droplets at $t = 0$ (Figure SI 10 in [38]) was plotted

217 against final ThT fluorescence readings at $t = 24$ hours, representing the relative amount of amyloid

218 aggregates formed (**Figure 3**C). We found a proportional correlation (linear R_2 of 0.43) between

219 the initial turbidity and the final ThT fluorescence readings (**Figure 3**C). This result implies that

220 LLPS-HS causally triggers amyloid formation. In contrast, electrostatically driven LLPS neither

221 promotes RNA-assisted tau aggregation, nor prevents heparin-induced tau aggregation as shown

222 in **Figure 3**C and **Figure 3-figure supplement 1**, and as previously reported [38]. These results

223 show that the strong correlation between LLPS and amyloid aggregation is unique to

224 hydrophobically-driven LLPS, as represented by LLPS-HS, while LLPS-ED and aggregation are

225 independent processes.

226 We further studied the effects of the frontotemporal dementia-related mutation P301L of

227 tau on the correlation between LLPS-HS and aggregation. Our data showed that tau187P301L

228 shows an even steeper dependence of the final ThT fluorescence intensity to the initial droplet

229   quantity at $t = 0$ (**Figure 3**C), implying that for a similar initial volume of droplets, tau187P301L

230   generates higher quantities of cross β-sheet structures, resulting in higher ThT fluorescence

231   intensity. Meanwhile, an analysis of the aggregation half time showed that in all examined

232   conditions P301L has significantly shortened the half time (**Figure 6-figure supplement 2**). These

233   results showed that P301L promotes tau aggregation under LLPS-HS conditions, consistent with

234   its broadly known aggregation-promoting properties under various *in vitro* and *in vivo* conditions.

235   Similar results were observed with 2N4R (**Figure 6-figure supplement 1**).

236

237   **Dehydration facilitates hydrophobically driven LLPS-HS**

238

239   To reveal the mechanisms that promote the transition of tau from high salt droplet to tau in fibrils,

240   we next focused on investigating the driving forces for tau to form in LLPS-HS. The dissolution

241   by 1,6-HD showed high salt droplets to be held together by hydrophobic interaction (**Figure 1**D).

242   When increasing the amount of 1,6-HD, we found the minimum [NaCl] to induce LLPS-HS to

243   shift significantly towards higher NaCl concentration (**Figure 4-figure supplement 3**C). This

244   implies that a greater amount of salt is needed to restore the same enhancement of hydrophobic

245   interactions that are disrupted by 1,6-HD.

246

247   Turbidity shows LLPS-HS is favored at higher temperature, following lower critical

248   saturation temperature behavior (LCST) (**Figure 2-figure supplement 1**A, C). This suggests that

249   free energy for LLPS-HS is rendered negative ($\Delta G < 0$) by a dominant and positive entropy term,

250   TΔS, according to $\Delta G = \Delta H - T\Delta S$. LCST behavior is seen when phase separation is accompanied

251   by an increase in total entropy (i.e. $\Delta S > 0$) that, as a result, leads to an increasingly dominant and

252   positive entropy (TΔS) term at higher temperature. The temperature at which $\Delta G = 0$ is then the

253   phase transition temperature, cloud point T_{cp}, above which phase separation occurs spontaneously.

254   Interestingly, either increasing [NaCl] or increasing [tau] lowers the T_{cp} above which LLPS-HS

255   occurs (**Figure 4-figure supplement 1**). This finding suggests that both the addition of salt and

256   higher tau concentration contribute to entropy gain upon LLPS. When adding PEG as a molecular

257   crowder, we observed that the minimum [NaCl] necessary to induce LLPS-HS also shifted towards

258   lower concentrations (**Figure 4-figure supplement 3**B). A recent study by Park et al.

259   demonstrated that PEG increases the entropy term upon LLPS by dehydration, and so enhances

260   LLPS without partitioning into the dense phase of LLPS [30]. Taken together, our results are

261   consistent with NaCl and PEG both sequestering water, and hence depleting the protein system of

262   free water in a process known as salting out [41], [59]. Dehydration of the tau-water system will

263   facilitate hydrophobic interactions and subsequent condensation by an increase of the entropic

264   term T∆S.

265

266   While the observations made by systematic changes in [NaCl], [tau], [PEG] and

267   temperature is consistent with dehydration- and entropy-driven LLPS-HS, a more direct

268   observation of dehydration is more satisfying. To measure the effect of dehydration near the tau

269   protein surface, we labeled tau with unpaired electron spin labels to perform electron spin envelope

270   echo modulation (ESEEM) and Overhauser dynamic nuclear polarization (ODNP) measurements.

271   ESEEM measures the relative changes in the local water density within a ~3-6 Å shell around a

272   spin label [60], [61], while ODNP measures water accessibility [62] and translational diffusivity

273   within a shell of ~5-10 Å [63], [64] (**Figure 4**A).

274

275   We labeled tau187 with MTSL on site 313 within the R3 domain and dissolved it into a

276   deuterium-based buffer. The magnitude of the ESEEM deuterium peak intensity dropped by over

277   20%, immediately upon addition of NaCl that led to the formation of high salt droplets (**Figure**

278   **4**B). This result represents a significant reduction of local water density near site 313.

279

280   We furthermore carried out ODNP relaxometry measurements to determine the cross-

281   relaxivity parameter k_σ, for tau187 at sites 303, 313, 322 and 404, representing the 4R domain and

282   the C-terminal region of tau. The k_σ value reflects on local water accessibility and/or translational

283   diffusivity within ~1 nm of the spin label (Eq. 5 of [65]). We found that the value of k_σ dropped

284   from 31 - 56 $M^{-1}s^{-1}$ to 9 - 23 $M^{-1}s^{-1}$ for all four sites as soon as high salt droplets formed (see per

285   site trend in **Figure 4**C). Note that k_σ measured on the free radical 4-hydroxyl-TEMPO was

286   unchanged upon addition of salt at concentrations that induce LLPS-HS (**Figure 4**C). Therefore,

287   the decrease of k_σ observed reflects a change in hydration properties near the tau protein surface

288   upon LLPS-HS formation. The reduction of the deuterium peak magnitude in ESEEM at site 313

289   shows that the reduction of water accessibility contributes to the drop of k_σ. Given the ~25%

290   reduction of deuterium peak magnitude together with the 50~80% drop in k_σ (**Figure 4**, **Figure 4-**

291 **source data 1**), it is reasonable to assume that it reflects, in addition to local dehydration, a

292 significant slowdown of surface water diffusivity near the microtubule binding domain and C-

293 terminal of tau when condensed into LLPS-HS. Strikingly, k_σ remains unchanged upon formation

294 of tau-RNA LLPS-ED (**Figure 4**C), showing that dehydration of LLPS-internal water is a

295 characteristic associated with hydrophobically driven LLPS-HS, but not of LLPS-ED.

296

297 **Dehydration reduces tau dynamics and triggers oligomer formation**
298

299 To study the dynamics of tau within high salt droplets, we carried out continuous wave

300 (cw) EPR spectroscopy. We labeled tau187 at four different sites: 303, 313, 322 and 404, and

301 extracted the rotational correlation times of the tethered spin label, t_R, from fitting the cwEPR

302 lineshape (see Materials and Methods). The value for t_R of the tethered spin reflects on the local

303 protein mobility, as the spin label is tethered to the protein side chain with steric constraints [66].

304 We first looked at t_R of the four sites before and after forming LLPS-HS. We found that LLPS-HS

305 formation results in dramatic changes in the spectral lineshape of the spin labeled tau (**Figure 5**A,

306 **Figure 5-figure supplement 2**). We used the microscopic order macroscopic disorder (MOMD)

307 model [67] with incremental complexity to fit the cw EPR lineshapes, using the MultiComponent

308 program developed by Christian Altenbach. At [NaCl] = 0–1.5 M (no droplets), lineshapes of the

309 samples were well fit with one isotropic t_R component (**Figure 5-figure supplement 2**). Increasing

310 [NaCl] to 3 M and above resulted in LLPS-HS. The lineshape of the samples deviated from the

311 one component fit, and required an additional mobility component (**Figure 5-figure supplement**

312 **1**A). The extracted t_R and the population of each component is represented in **Figure 5**B as a

313 function of salt concentration. We found that t_R of the second component was significantly higher

314 than for the first component (i.e. slower dynamics), for all sites. The second component

315 represented 65-96% of the spin label population above 3 M NaCl (**Figure 5-source data 1**).

316 Meanwhile, increasing [NaCl] up to 4.5 M alone does not change the lineshape of the free radical

317 4-hydroxyl-TEMPO (**Figure 5-figure supplement 4**), showing the effects of high salt

318 concentration do not change the rotational dynamics of the spin itself. We hypnotize that this

319 increase of rotational correlation time t_R reflect on the formation of higher molecular weight

320 assemblies, i.e. oligomers. These results imply that the dynamics of the majority of tau proteins,

321 reported on via protein-tethered spin labels, is slowed down in the LLPS-HS state. In addition to

322 the slowed rotational dynamics, we found emergence of rotational anisotropy in the second

323 component for [NaCl] above 4 M. The presence of anisotropy indicates that the tethered spin label

324 is highly restricted [67], [68], likely from steric hindrance of nearby tau protein, suggesting that

325 tau starts to more tightly pack into protein assembly at very high salt concentration.

326

327 Next, we endeavor to show whether the formation of these oligomer species, revealed by

328 slow label dynamics, originates from high salt concentration or from LLPS itself. First, in the

329 absence of high salt droplets, we observed that the lineshape of cw EPR spectra of the tau-tethered

330 spin label broadened upon NaCl addition, giving an average t_R of ~450 ps without NaCl and ~600

331 ps at 1.5M, at all sites (**Figure 5-source data 1**). In addition, at constant [NaCl] we titrated [HD]

332 from 0% to 10%, where [HD] above 2% eliminated droplets. CwEPR lineshape analysis showed

333 that the correlation time was neither abruptly nor distinctly reduced in the absence of droplets

334 above 2% HD (**Figure 5-figure supplement 3**). These results show that the drastic reduction in

335 protein dynamics, which we hypothesized to reflect on the formation of oligomers, originate from

336 dehydration by concentrated salt, only indirectly by LLPS.

337

338 **P301L promotes hydrophobic interactions**

339

340 One of the mysteries in tau amyloid aggregation is how a single site mutation, e.g, P301L,

341 dramatically promotes the aggregation propensity of a protein of hundreds of amino acids. We

342 propose here a plausible mechanism. We utilize LLPS-HS as a tool to measure hydrophobic

343 interactions among tau. We studied the effects of the P301L mutation on LLPS-HS propensity.

344 We measured turbidity of tau187 with and without P301L mutation under the exact same

345 conditions. Turbidity from independent biological repeats showed that in the presence of an

346 intermediate salt concentration of 3.25 M, the presence of P301L mutation significantly promoted

347 LLPS-HS formation (**Figure 6**B). In other words, the P301L mutation lowers the [NaCl] threshold

348 required to induce LLPS-HS. Representative microscope images, shown in **Figure 6**A, confirmed

349 that P301L promotes high salt droplet formation. These results suggest that the P301L mutation

350 promotes hydrophobic interactions among tau proteins, in agreement with previous proposal that

351 P301L mutation extends local conformation, hence reveals the hydrophobic hexapeptide

352 $_{306}$VQIVYK$_{311}$ [69]. However, whether the increased hydrophobicity of tau in the presence of

353 P301L is solely due to conformational changes or other biophysical factors requires in-depth

354 studies in the future. In addition, we observed that the ThT activity triggered by LLPS-HS (shown

355 in **Figure 3** for wild type (WT)) increases further for P301L compared to WT (**Figure 6**C). This

356 enhanced ThT fluorescence for P301L mutant is most likely a combination of both the promotion

357 of droplet formation (which in turn triggers ThT-sensitive aggregation) and a high aggregation

358 propensity that facilitate the droplet to fibril transition.

Discussion

360 Protein liquid-liquid phase separation in pathological contexts have led to intense investigation in

361 the recent past. In particular, tau LLPS has been studied in several reports leading to contrasting

362 hypothesis whether or not LLPS directly triggers amyloid aggregation. We address in this study

363 two key questions: (1) Is tau LLPS of a universal type or could droplets formed in different

364 conditions possess different properties? (2) Is there a direct cause-and-effect relationship between

365 LLPS and aggregation?

366

367 In this report, we have shown that tau at high salt concentration is capable of forming LLPS

368 (referred to as LLPS-HS) driven by hydrophobic interactions. High NaCl concentrations both

369 screen electrostatic interactions and sequester water away from the protein, thereby amplify the

370 effect of hydrophobic association of tau. The concentration of salt needed to achieve LLPS of tau

371 of the order of ~3M is not physiological by any means. However, the influence of such condition

372 on the proteins or biopolymers, i.e. strong electrostatic screening and amplified hydrophobic

373 attraction can easily represent physiologically relevant state. For example, tau under conditions of

374 significant phosphorylation and acetylation would experience effects similar to that of screening

375 the net positive charge effects of the many lysine residues lining on the tau surface, while strong

376 hydrophobic attraction was proposed to be at the origin of hyperphosphorylated tau aggregation

377 [70].

378

379 Using EPR spectroscopy, FILM and biochemical assays, we showed that LLPS-HS exhibit slowed

380 local dynamics, restricted water accessibility, elevated microviscosity, as well as irreversible

381 maturation, in stark contrast to electrostatically driven LLPS-ED. Many different conditions can

382 facilitate tau LLPS, but this study shows that the classification of hydrophobically or

383 electrostatically driven LLPS might be an effective framework to classify tau droplets and predict

384 their properties or effects on aggregation. We used tau-RNA complex coacervation to showcase

385 LLPS-ED, but as shown in **Figure 1**D and elsewhere [33], [34], both complex and simple

386 coacervation can form LLPS-ED.

387

388 Establishing a causal relationship between LLPS and protein aggregation is challenging because

389 the two processes can occur under identical conditions without necessarily being dependent [38].

390 Importantly, under conditions where both phenomena occur, it is tempting to deduce a cause-and-

391 effect relationship. Firstly, droplets can form and dissolve within seconds to minutes, while

392 aggregation occurs on the timescale of hours to days, therefore the sequential occurrence of

393 droplets then aggregates does not necessarily imply LLPS is an intermediate state towards

394 aggregation. Secondly, droplets, by definition, increase protein concentration. Therefore, even if

395 both phenomena were completely independent, one would observe aggregates slowly forming in

396 the inside of pre-existing droplets, merely because it is where the protein is, which might lead to

397 the wrong conclusion that droplets directly *trigger* aggregation. In our opinion, a robust way to

398 establish causation between droplets and aggregates is to examine multiple conditions across the

399 LLPS phase boundary, and correlate the changes of droplet volume to the change of fibril mass.

400 Using this approach, we have shown in [38] that although tau-cofactor LLPS-ED and amyloid

401 aggregation are concomitant in many conditions, they are biophysically independent processes. In

402 this study, we show that hydrophobically driven LLPS-HS is different, and that LLPS-HS of tau

403 trigger amyloid formation (**Figure 3**C and **Figure 3-figure supplement 3**).

404

405 Previous reports on tau LLPS made with K18 at low salt concentrations showed that the droplets

406 were dissolved above ~200 mM NaCl and at 3 % HD, suggesting that a combination of

407 electrostatic and hydrophobic driving forces were holding the liquid condensed state together [19],

408 [51]. These droplets were not reported to evolve spontaneously to ThT-active species. In contrast,

409 droplets formed by hyperphosphorylated 2N4R in Wegmann *et al*. [20] were shown to evolve to

410 amyloid fibrils and to be insensitive to [NaCl]>1M, but to be sensitive to 10% HD, showing that

411 they are driven mostly by hydrophobic interactions. These results together with our work suggest

412 a general mechanism that hydrophobically-driven droplets promote aggregation.

413

414   We have shown that the local environment in the high salt droplets is drastically different from the

415   one in tau LLPS-ED droplets. FLIM showed that, initially after high salt droplet formation, i.e.

416   even in the absence of significant aging, the micro-viscosity is significantly higher in LLPS-HS

417   than in LLPS-ED droplets. Furthermore, ESEEM and ODNP measurements revealed that water

418   accessibility and water dynamics is significantly more retarded in LLPS-HS than in LLPS-ED.

419   These properties found in LLPS-HS are favorable to protein aggregation because amyloid

420   formation requires a critical step of dehydration, where even hydrophilic residue must give up their

421   ideal hydration to pack into cross-β sheets and steric zippers. Besides, amyloid fibers form a solid-

422   like matrix of high viscosity. We suggest that the features of high viscosity, perturbed protein

423   dynamics and dehydration are general hallmarks of protein LLPS on-pathway to aggregation.

424

425   Cw EPR linseshape analysis provides a mechanistic view of tau aggregation through LLPS-HS.

426   We found that increasing the concentration of salt progressively triggers the formation of high

427   order oligomers, as evidenced by a long rotational correlation time of the spin labels tethered to

428   tau. These oligomers are observed even at medium [NaCl] (e.g. 1.5 M) where droplets are not

429   present. An analysis of the dipolar broadening of the cwEPR spectra (**Figure 5-figure supplement**

430   **4**) shows the absence of specific packing (such as in-register cross-β sheets or steric zipper

431   structures) in these ThT-inactive oligomers. LLPS seems however necessary and sufficient to

432   convert these oligomers into ThT-active species and eventually amyloid fibers, as shown by the

433   direct correlation between ThT fluorescence and droplet amount (**Figure 3**C).

434

435   Finally, we demonstrate that the disease-associated mutation P301L promotes both LLPS-HS and

436   amyloid formation (**Figure 6**). Conversely, P301L mutation has no influence on the formation of

437   LLPS-ED [38]. Therefore, we can conclude that P301L mutation promotes intermolecular

438   hydrophobic interactions that drives LLPS-HS. Furthermore, the correlation plots shown in **Figure**

439   **3**C and **Figure 6-figure supplement 2**C show that at similar droplet quantity, P301L mutant will

440   form greater quantity of ThT active species, and does so more rapidly than tau WT. The

441   aggregation-promoting effect of P301L is well known and elegant explanations have been

442   suggested recently [69, p. 201]. Here, we show that the P301L mutation exerts two seemingly

443   independent effects that both ultimately increase aggregation: (i) It promotes local hydrophobic

444   interactions, thereby promoting hydrophobically-driven phase separation, which in turn triggers

445 aggregation and (ii) promotes aggregation-prone conformations, in particular by exposing
446 amyloidogenic segments PHF6(*), independently of LLPS formation. Other disease-related
447 mutations might not combine these effects, because they do not modulate the accessibility of the
448 hydrophobic PHF6(*) segments, explaining why P301L is particularly potent at promoting fibril
449 formation under wide experimental conditions, from *in vitro*, in cells and *in vivo* mouse models.

450

451 In conclusion, this study uncovers that there is a clear cause-effect relationship between LLPS and
452 aggregation of tau, only when LLPS is driven by hydrophobic association of tau that we found to
453 be preceded by dehydration of its interfacial water. Different physical or biological factors can
454 drive hydrophobically driven LLPS. While this study showcases the principle by relying on
455 dehydration-promoting salting-out mechanisms induced at high [NaCl] concentration, we posit
456 that hydrophobically driven LLPS can be exerted by many other factors of pathological
457 significance, including the posttranslational modification of tau that can mute the strong positive
458 surface charge density from the abundant lysine residues on tau, e.g. by acetylation and
459 phosphorylation, or enhanced intracellular osmotic crowding pressure, as well as certain
460 pathological mutations of tau, with P301L representing one prominent example. Hence, the liquid
461 condensed state of tau that can be seen *in vitro* and intra cellularly may be a mediating mechanism
462 by which tau can be sequestered and initially protected from aggregation if LLPS can be reversed,
463 or is inadvertently and irreversibly on pathway towards a pathological state.

Acknowledgements

474

Materials and Methods

Tau proteins expression and purification

Both full length human tau (2N4R) and its N-terminal truncated, microtubule binding domain contained variant tau187 (residues 255-441 with a His-tag at the N-terminus) were used for *in vitro* studies. The cloning, expression, and purification of both 2N4R and tau187 have been previously described [71], [72]. The cysteine-free variants of both 2N4R and tau187 (C291SC322S) were generated via site-direct mutagenesis.

E. coli BL21 (DE3) cells previously transfected were cultured from frozen glycerol stock overnight in 10 mL luria broth (LB) which was used to inoculate 1 L of fresh LB. Culturing and inoculation were performed at 37 °C with shaking of 200 rpm. At OD_{600} of 0.6–0.8. After cell growth, 2N4R culture was incubated with 500 mM NaCl and 10 mM betaine before inducing expression. Both 2N4R and Tau187 variant expressions were induced by incubation with 1 mM isopropylß-D-thiogalactoside (Sigma Aldrich) for 2–3 h. Cells were harvested by centrifugation for 10 min at $6000 \times g$ (Beckman J-10; Beckman Instruments, Inc.), and the pellets were stored at −20 °C until further use.

Cell pellets were resuspended in lysis buffer (Tris-HCl pH 7.4, 100 mM NaCl, 0.5 mM DTT, 0.1 mM EDTA, 1mM PMSF) with 1 Pierce protease inhibitor tablet (Thermo Fisher, EDTA-Free). Lysis was initiated by the addition of lysozyme (2 mg/ml), DNase (20 µg/ml), and $MgCl_2$ (10 mM) and incubated on an orbital shaker for 30 min in room temperature. Lysate was then heated to 65 °C for 13 min, cooled on ice for 20 min and then centrifuged to remove the precipitant. The supernatant was loaded onto a Ni-NTA agarose column pre-equilibrated with wash buffer A (20 mM sodium phosphate pH 7.0, 500 mM NaCl, 10 mM imidazole, 100 µM EDTA). The column was then washed with 20 ml of buffer A, 15 ml buffer B (20 mM sodium phosphate pH 7.0, 1 M NaCl, 20 mM imidazole, 0.5 mM DTT, 100 µM EDTA). Purified tau was eluted with buffer C (20 mM sodium phosphate pH 7.0, 0.5 mM DTT, 100 mM NaCl) supplemented with varying amounts of imidazole increasing from 100 mM to 300 mM. The protein was then concentrated via centrifugal filters (MWCO 10 kDa; Millipore Sigma) and the buffer was exchanged into final buffer by PD-10 desalting column (GE Healthcare). The final protein concentration was determined by UV-Vis absorption at 274 nm using an extinction coefficient of 2.8 $cm^{-1}mM^{-1}$ for tau187 and 5.8 $cm^{-1}mM^{-1}$ for 2N4R, calculated from absorption of Tyrosine [3]. Same purification protocols were used for both 2N4R and tau187.

Bright field microscopy and TEM imaging

To confirm the occurrence of LLPS and the formation of liquid droplets, bright field microscope images were taken immediately after sample preparation, using an inverted compound microscope (Zeiss Axtrovert 200M).

For TEM imaging 10 µL of recombinant tau fibril samples were applied to copper grid (Electron Microscopy Science, FCF-300-Cu) cleaned with plasma for 20 s. Samples were stained with 10

518 µL 1.5 w/v % uranyl acetate. Grids were then imaged with a JEOL JEM-1230 (JEOL USA, Inc)
519 at the indicated magnifications.
520

Turbidity measurements

523 Turbidity of samples at varying [NaCl] were represented by OD_{500} measured using a plate reader
524 (Bio-Tek Synergy 2) and 384-well microplate (Corning 3844). To minimize the inference of ThT
525 fluorescence and tau fibril scattering, averaged absorbance of the initial 10 min where ThT
526 fluorescence is below 10% was used as turbidity reading.

528 Turbidity of samples at ramping temperatures were represented by OD_{500} measured using Jasco J-
529 1500 CD Spectrometer (JASCO Inc.) equipped with temperature controller and spectrophotometer.
530 120 µL of tau in designated conditions were prepared in a 100 µL cuvette (Starna Scientific Ltd)
531 and kept at 4 °C for 5 min before cycling. Heating and cooling temperatures were ramped at
532 1 °C/min while OD_{500} was monitored.

ThT assay and half time analysis

536 LLPS samples were prepared onto a 384-well microplate with additional 1 µM Thioflavin T. ThT
537 fluorescence was read from a plate reader (Bio-Tek Synergy 2, excitation 440/30, emission 485/20,
538 number of flash 16). Data was processed using R package gen5helper following the previous
539 reported methods to reduce artifacts caused by the lamp fluctuation [38].

541 We followed the previously reported methods [38] to extract the half time and maximum ThT
542 fluorescence, by scaling ThT fluorescence to 0 to 1 and fitting to a sigmoid function,

$$y = \frac{A}{1 + \exp(-k(t - t_{1/2}))}$$

544 where the fitted A and $t_{1/2}$ were used as maximum ThT fluorescence and half time, respectively.
545 Fitting results were filtered by $p < 0.05$ to ensure a good fit.

Synthesis of BODIPY-NHS Dye

549 BODIPY-NHS was synthesized as previously described with few modifications [55]. A brief
550 description for the synthesis of BODIPY-NHS dye is provided in **Figure 2-figure supplement 3**
551 and full details can be found at DOI:10.6084/m9.figshare.12746756. BODIPY-NHS can be
552 synthesized in six steps starting from 4-hydroxybenzaldehyde. In the first step, etherification of 4-
553 hydroxybenzaldehyde by potassium carbonate and ethyl 4-bromobutyrate afforded ethyl 4-(4-
554 formylphenoxy)butyrate **(1)** in 98% yield. Then, hydrolysis with potassium hydroxide provided 4-
555 4(formyl-phenoxy)butyric acid **(2)** in 96% yield. In order to overcome solubility issues that the
556 carboxylic acid intermediate presents in pyrrole, used in step 4, it was converted to the
557 corresponding silyl ester. It reacted with tert-butyl(chloro)diphenylsilane in a reaction promoted
558 by triethyl amine and 4-dimethylaminopyridine affording tert-butyldiphenylsilyl 4-(4-
559 formylphenoxy)butanoate **(3)** in 68% yield. The aldehyde **(3)** was then treated with TFA (12 mol%)
560 and an excess of pyrrole under solvent-free conditions providing the dipyrromethane **(4)** in 66%
561 yield. Oxidation with 2,3-dichloro-5,6-dicyano-1,4-benzoquinone followed by reaction with

562 BF$_3$·OEt$_2$ and triethylamine lead to BODIPY-COOH in 36% yield. Steglich esterification with N-
563 hydroxysuccinimide yielded BODIPY-NHS (64% yield).

564
565

Conjugation of BODIPY-NHS to 2N4R

566
567

568 2N4R protein was diluted to a concentration of 20 µM in a PBS buffer. 20 mM BODIPY dissolved
569 in DMSO was added to the protein to a final concentration of 20 µM. The solution was stirred at
570 room temperature for 4 hours and any unreacted BODIPY-NHS was quenched by adding a
571 solution of excess glycine. The unreacted dye was separated from the conjugated protein with a 7k
572 MWCO Zeba™ Spin Desalting Column equilibrated with a 20 mM HEPES buffer, pH = 7.0. The
573 conjugated protein was concentrated in an 3K MWCO Amicon Ultra Spin Column to a final
574 concentration of approximately 500 µM. Protein concentration was determined with a Pierce
575 Assay, while the amount of conjugated dye present was calculated by measuring its absorbance at
576 510 nM. Typical labeling reactions gave a 1:1 labeling efficiency.

577

Measurement and Analysis of FLIM Spectra

578
579

580 All FLIM measurements were made on a Leica SP8 FALCON Resonant Scanning Confocal
581 Microscope equipped with TCSPC. Images were recorded such that each pixel had a minimum of
582 1000 photons collected. All data analysis was performed with FLIMFIT [73]. As observed
583 previously [58], lifetime decay curves required multiexponential fits. We found that the higher
584 lifetime component of a 2-exponential fit tracked well with control viscosity measurements made
585 in varying glycerol concentrations and as such it was used for all subsequent analysis.

586

CwEPR and lineshape analysis

587
588

589 In this report, we used four variants of tau187 for cwEPR, ODNP and ESEEM studies:
590 tau187/C291S/C322S/S303C,   tau187/C291S/C322S/G313C,   tau187/C291S,
591 tau187/C291S/C322S/S404C, with one cysteine at site 303, 313, 322 and 404, respectively.

592

593 We followed the previous reported methods [38] for spin labeling, cwEPR acquisition, and
594 lineshape analysis. For spin labeling, the freshly eluted variants above were replaced in 20 mM
595 HEPES pH 7.0, using a PD-10 desalting column (GE Healthcare). Protein after PD-10 was labeled
596 overnight at 4°C by immediately mixing with a 10-fold molar excess of the spin label (1-oxyl-
597 2,2,5,5-tetramethylpyrroline-3-methyl) methanethiosulfonate (MTSL; Toronto Research
598 Chemicals), resulting in spin labelled tau at designated site. Excess label was removed using PD-
599 10. The protein was concentrated using centrifugal filter (MWCO 10 kDa; Amicon) and the final
600 protein concentration was determined by UV-Vis absorption at 274 nm as mentioned above.
601 Cystein-free non-labeled tau187C291SC322S was used in order to achieve spin dilution.

602

603 Cw EPR measurements were carried out using a X-band spectrometer operating at 9.8 GHz (EMX;
604 Bruker Biospin, Billerica, MA) and a dielectric cavity (ER 4123D; Bruker Biospin, Billerica, MA).
605 Spin labeled tau187 was mixed with tau187C291SC322S at 1:4 molar ratio to reach 20% spin
606 labeling. A sample of 4.0 µl volume was loaded into a quartz capillary (CV6084; VitroCom) and
607 sealed at both ends with critoseal, and then placed in the dielectric cavity for measurements. Cw

608 EPR spectra were acquired by using 1.8 mW of microwave power, 0.5 gauss modulation amplitude,
609 100 gauss sweep width, and 8-64 scans for signal averaging.
610
611 The recorded cw EPR spectra were fit with simulation using models with incremental complexity.
612 EPR simulation and fitting were performed using MultiComponent, a program developed by
613 Christian Altenbach (University of California, Los Angeles). For all spectra fitting, the magnetic
614 tensors A and g were fixed and used as constraints as previously reported [74]. These values are
615 A_{xx} = 6.2 G, A_{yy} = 5.9 G, A_{zz} = 37.0 G, and g_{xx} = 2.0078, g_{yy} = 2.0058, and g_{zz} = 2.0022. For
616 soluble tau and tau at [NaCl] < 2.0 M, the cw EPR spectra of all four spin-labeled tau variants were
617 best fitted with a single isotropic component simulation and the rotational diffusion constant (R)
618 can be extracted. The rotation correlation time τ_R was calculated using $\tau_R = 1/(6R)$. For tau at 2.0
619 M < [NaCl] < 4.0 M, the single isotropic component simulation failed to capture the lineshape
620 (**Figure 5-figure supplement 1**A). A second isotropic component was added to increase the
621 complexity of the model. The second isotropic component were set to be identical to the first
622 component, except with an independent R value. The fitting parameters were limited at a minimum,
623 which includes the population, p and the rotational diffusion constants of the first and second
624 isotropic component R_1 and R_2. For tau at [NaCl] > 4.0 M, both the signal and double isotropic
625 component simulation failed to capture the lineshape (**Figure 5-figure supplement 1**B).
626 Anisotropic parameters were added to the second components and subjected to fit. The fitting
627 parameters include p, R_1, R_2, and the added parameters for the second components including the
628 tilt angle of the diffusion tensor α_D, β_D, orienting potentials c_{20}, c_{22}, c_{40}, c_{44}. Fitted spectra and
629 parameters of all four sites at different [NaCl] are shown in **Figure 5-figure supplement 2** and
630 **Figure 5-source data 1**, respectively.
631
632 **Overhauser dynamic nuclear polarization (ODNP)**
633
634 We used the aforementioned four spin labeled tau187 variants (singly labeled on site 303, 313,
635 322 and 404, respectively), and followed previously reported methods for ODNP experiments [30].
636 100 µM spin labeled tau187 was mixed with designated concentration of NaCl. Immediately after
637 sample preparation, 3.5 µL of the samples were loaded into quartz capillaries of 0.6 mm
638 ID × 0.84 mm OD (Vitrocom, New Jersey, USA), and two ends of the tubes were sealed with
639 Critoseal and beeswax respectively. ODNP experiments were performed using a Bruker EMXPlus
640 spectrometer and a Bruker Avance III NMR console (Bruker, Massachusetts, USA). The capillary
641 tube was mounted on a home-built NMR probe with a U-shaped NMR coil, and was set in a Bruker
642 ER 4119HS-LC sensitivity cavity. Samples were irradiated at 9.8 GHz with the center field set at
643 3484 G and sweep width of 120 G. Dry air was kept at temperature of 18 ºC and purged through
644 the NMR probe during all measurements. ODNP data was analyzed using customized python
645 script WorkupODNP and ODNPLab, available on https://www.github.com. Theory of ODNP and
646 details in the experiment are previously reported in other studies [63], [64].
647
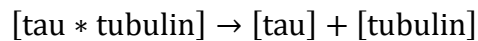648 **3-Pulse Electron Spin Echo Envelope Modulation (ESEEM)**
649
650 We followed previously reported methods for ESEEM measurements [75]. ESEEM measurements
651 were performed at X-Band on an ELEXSYS E580 spectrometer at 80 K with an Oxford
652 instruments cryostat (CF935P) and temperature controller (ITC503). A Bruker MS3 resonator was
653 maximally overcoupled to a Q-factor of approximately 100 for these measurements. Immediately

654 after sample preparation, 35 μL of sample was loaded into a 3 mm OD quartz EPR tube and flash
655 frozen in liquid nitrogen before being inserted into the resonator. Spin labeled tau187 at site 313
656 was used for measurement. All experiments were carried out in deuterated 20 mM HEPES with
657 20 wt% Ficoll.
658
659 The ESEEM data was fit by 5_{th} order polynomial to correct the background decay, hamming
660 windowed, zero-filled and Fourier-transformed, following reported method [75]. We interpreted
661 the reduce of the the intensity of the deuterium peak as a result of dehydration near the site 313.
662 Raw data was shown in **Figure 4-figure supplement 2**.
663

664 **Estimate Unbound Tau Concentration**
665

666 Assuming tau binding to microtubule has a stoichiometry of 1:1 between tau molecule and tubulin
667 monomer, regardless of different types of tubulin monomers, the dissociation process can be
668 expressed as
669 $$[\text{tau} * \text{tubulin}] \rightarrow [\text{tau}] + [\text{tubulin}]$$
670 where [tau*tubulin] and [tau] represent the bounded and unbounded tau concentration,
671 respectively. Knowing
672 $$K_d = \frac{[\text{tau}] + [\text{tubulin}]}{[\text{tau} * \text{tubulin}]} \approx 10^{-7}\text{M}$$
673 $$[\text{tau}] + [\text{tau} * \text{tubulin}] \approx 10^{-6}\text{M}$$
674 $$[\text{tubulin}] + [\text{tau} * \text{tubulin}] \approx 4 \times 10^{-5}\text{M}$$
675 one can solve for unbound tau concentration $[\text{tau}] \approx 3$ nM
676
677

References

[1] T. Guo, W. Noble, and D. P. Hanger, "Roles of tau protein in health and disease," *Acta Neuropathol. (Berl.)*, vol. 133, no. 5, pp. 665–704, 2017, doi: 10.1007/s00401-017-1707-9.

[2] J. Avila, J. J. Lucas, M. Perez, and F. Hernandez, "Role of tau protein in both physiological and pathological conditions," *Physiol. Rev.*, vol. 84, no. 2, pp. 361–384, Apr. 2004, doi: 10.1152/physrev.00024.2003.

[3] J. Q. Trojanowski, T. Schuck, M. L. Schmidt, and V. M. Lee, "Distribution of tau proteins in the normal human central and peripheral nervous system," *J. Histochem. Cytochem. Off. J. Histochem. Soc.*, vol. 37, no. 2, pp. 209–215, Feb. 1989, doi: 10.1177/37.2.2492045.

[4] M. Ackmann, H. Wiech, and E. Mandelkow, "Nonsaturable Binding Indicates Clustering of Tau on the Microtubule Surface in a Paired Helical Filament-like Conformation," *J. Biol. Chem.*, vol. 275, no. 39, pp. 30335–30343, Sep. 2000, doi: 10.1074/jbc.M002590200.

[5] G. Hiller and K. Weber, "Radioimmunoassay for tubulin: a quantitative comparison of the tubulin content of different established tissue culture cells and tissues," *Cell*, vol. 14, no. 4, pp. 795–804, Aug. 1978, doi: 10.1016/0092-8674(78)90335-5.

[6] H. Ksiezak-Reding, L. I. Binder, and S. H. Yen, "Immunochemical and biochemical characterization of tau proteins in normal and Alzheimer's disease brains with Alz 50 and Tau-1.," *J. Biol. Chem.*, vol. 263, no. 17, pp. 7948–7953, Jun. 1988, Accessed: May 31, 2019. [Online]. Available: http://www.jbc.org/content/263/17/7948.

[7] N. Gustke, B. Trinczek, J. Biernat, E.-M. Mandelkow, and E. Mandelkow, "Domains of tau Protein and Interactions with Microtubules," *Biochemistry*, vol. 33, no. 32, pp. 9511–9522, Oct. 1994, doi: 10.1021/bi00198a017.

[8] T. Arendt, J. T. Stieler, and M. Holzer, "Tau and tauopathies," *Brain Res. Bull.*, vol. 126, pp. 238–292, Sep. 2016, doi: 10.1016/j.brainresbull.2016.08.018.

[9] C. P. Brangwynne, P. Tompa, and R. V. Pappu, "Polymer physics of intracellular phase transitions," *Nat. Phys.*, vol. 11, no. 11, pp. 899–904, Nov. 2015, doi: 10.1038/nphys3532.

[10] A. A. Hyman, C. A. Weber, and F. Jülicher, "Liquid-Liquid Phase Separation in Biology," *Annu. Rev. Cell Dev. Biol.*, vol. 30, no. 1, pp. 39–58, 2014, doi: 10.1146/annurev-cellbio-100913-013325.

[11] S. Alberti and S. Carra, "Quality Control of Membraneless Organelles," *J. Mol. Biol.*, vol. 430, no. 23, pp. 4711–4729, Nov. 2018, doi: 10.1016/j.jmb.2018.05.013.

[12] J. A. Toretsky and P. E. Wright, "Assemblages: Functional units formed by cellular phase separation," *J Cell Biol*, vol. 206, no. 5, pp. 579–588, Sep. 2014, doi: 10.1083/jcb.201404124.

[13] A. Molliex *et al.*, "Phase Separation by Low Complexity Domains Promotes Stress Granule Assembly and Drives Pathological Fibrillization," *Cell*, vol. 163, no. 1, pp. 123–133, Sep. 2015, doi: 10.1016/j.cell.2015.09.015.

[14] Y. R. Li, O. D. King, J. Shorter, and A. D. Gitler, "Stress granules as crucibles of ALS pathogenesis," *J Cell Biol*, vol. 201, no. 3, pp. 361–372, Apr. 2013, doi: 10.1083/jcb.201302044.

[15] T. Murakami *et al.*, "ALS/FTD Mutation-Induced Phase Transition of FUS Liquid Droplets and Reversible Hydrogels into Irreversible Hydrogels Impairs RNP Granule Function," *Neuron*, vol. 88, no. 4, pp. 678–690, Nov. 2015, doi: 10.1016/j.neuron.2015.10.030.

[16] A. Patel *et al.*, "A Liquid-to-Solid Phase Transition of the ALS Protein FUS Accelerated by Disease Mutation," *Cell*, vol. 162, no. 5, pp. 1066–1077, Aug. 2015, doi: 10.1016/j.cell.2015.07.047.

[17] Y. Chen and T. J. Cohen, "Aggregation of the nucleic acid-binding protein TDP-43 occurs via distinct routes that are coordinated with stress granule formation," *J. Biol. Chem.*, vol. 294, no. 10, pp. 3696–3706, 08 2019, doi: 10.1074/jbc.RA118.006351.

[18] S. Ray *et al.*, "Liquid-liquid phase separation and liquid-to-solid transition mediate α-synuclein amyloid fibril containing hydrogel formation," *bioRxiv*, p. 619858, Apr. 2019, doi: 10.1101/619858.

[19] S. Ambadipudi, J. Biernat, D. Riedel, E. Mandelkow, and M. Zweckstetter, "Liquid–liquid phase separation of the microtubule-binding repeats of the Alzheimer-related protein Tau," *Nat. Commun.*, vol. 8, no. 1, p. 275, Aug. 2017, doi: 10.1038/s41467-017-00480-0.

[20] S. Wegmann *et al.*, "Tau protein liquid-liquid phase separation can initiate tau aggregation," *EMBO J.*, vol. 37, no. 7, Apr. 2018, doi: 10.15252/embj.201798049.

[21] X. Zhang *et al.*, "RNA Stores Tau Reversibly in Complex Coacervates," *bioRxiv*, p. 111245, Feb. 2017, doi: 10.1101/111245.

[22] Y. Lin *et al.*, "Narrow equilibrium window for complex coacervation of tau and RNA under cellular conditions," *eLife*, vol. 8, p. e42571, Apr. 2019, doi: 10.7554/eLife.42571.

[23] A. Hernández-Vega *et al.*, "Local Nucleation of Microtubule Bundles through Tubulin Concentration into a Condensed Tau Phase," *Cell Rep.*, vol. 20, no. 10, pp. 2304–2312, Sep. 2017, doi: 10.1016/j.celrep.2017.08.042.

[24] J. C. Ferreon *et al.*, "Acetylation Disfavors Tau Phase Separation," *Int. J. Mol. Sci.*, vol. 19, no. 5, May 2018, doi: 10.3390/ijms19051360.

[25] A. Majumdar, P. Dogra, S. Maity, and S. Mukhopadhyay, "Liquid–Liquid Phase Separation Is Driven by Large-Scale Conformational Unwinding and Fluctuations of Intrinsically Disordered Protein Molecules," *J. Phys. Chem. Lett.*, vol. 10, no. 14, pp. 3929–3936, Jul. 2019, doi: 10.1021/acs.jpclett.9b01731.

[26] S. Park, S. Kim, Y. Jho, and D. S. Hwang, "Cation−π Interactions and Their Contribution to Mussel Underwater Adhesion Studied Using a Surface Forces Apparatus: A Mini-Review," *Langmuir*, Aug. 2019, doi: 10.1021/acs.langmuir.9b01976.

[27] S. F. Banani, H. O. Lee, A. A. Hyman, and M. K. Rosen, "Biomolecular condensates: organizers of cellular biochemistry," *Nat. Rev. Mol. Cell Biol.*, vol. 18, no. 5, pp. 285–298, May 2017, doi: 10.1038/nrm.2017.7.

[28] H. J. Dyson, P. E. Wright, and H. A. Scheraga, "The role of hydrophobic interactions in initiation and propagation of protein folding," *Proc. Natl. Acad. Sci.*, vol. 103, no. 35, pp. 13057–13061, Aug. 2006, doi: 10.1073/pnas.0605504103.

[29] B. Gabryelczyk *et al.*, "Hydrogen bond guidance and aromatic stacking drive liquid-liquid phase separation of intrinsically disordered histidine-rich peptides," *Nat. Commun.*, vol. 10, no. 1, pp. 1–12, Nov. 2019, doi: 10.1038/s41467-019-13469-8.

[30] S. Park *et al.*, "Dehydration entropy drives liquid-liquid phase separation by molecular crowding," *Commun. Chem.*, vol. 3, no. 1, pp. 1–12, Jun. 2020, doi: 10.1038/s42004-020-0328-8.

[31] S. L. Crick, K. M. Ruff, K. Garai, C. Frieden, and R. V. Pappu, "Unmasking the roles of N- and C-terminal flanking sequences from exon 1 of huntingtin as modulators of polyglutamine aggregation," *Proc. Natl. Acad. Sci. U. S. A.*, vol. 110, no. 50, pp. 20075–20080, Dec. 2013, doi: 10.1073/pnas.1320626110.

[32] S. Elbaum-Garfinkle *et al.*, "The disordered P granule protein LAF-1 drives phase separation into droplets with tunable viscosity and dynamics," *Proc. Natl. Acad. Sci. U. S. A.*, vol. 112, no. 23, pp. 7189–7194, Jun. 2015, doi: 10.1073/pnas.1504822112.

[33] S. Boyko, X. Qi, T.-H. Chen, K. Surewicz, and W. K. Surewicz, "Liquid-liquid phase separation of tau protein: The crucial role of electrostatic interactions," *J. Biol. Chem.*, p. jbc.AC119.009198, May 2019, doi: 10.1074/jbc.AC119.009198.

[34] V. Singh, L. Xu, S. Boyko, K. Surewicz, and W. K. Surewicz, "Zinc promotes liquid-liquid phase separation of tau protein," *J. Biol. Chem.*, p. jbc.AC120.013166, Mar. 2020, doi: 10.1074/jbc.AC120.013166.

[35] P. Li *et al.*, "Phase transitions in the assembly of multivalent signalling proteins," *Nature*, vol. 483, no. 7389, pp. 336–340, Mar. 2012, doi: 10.1038/nature10879.

[36] S. Kim *et al.*, "Complexation and coacervation of like-charged polyelectrolytes inspired by mussels," *Proc. Natl. Acad. Sci.*, vol. 113, no. 7, pp. E847–E853, Feb. 2016, doi: 10.1073/pnas.1521521113.

[37] T. J. Nott *et al.*, "Phase Transition of a Disordered Nuage Protein Generates Environmentally Responsive Membraneless Organelles," *Mol. Cell*, vol. 57, no. 5, pp. 936–947, Mar. 2015, doi: 10.1016/j.molcel.2015.01.013.

[38] Y. Lin, Y. Fichou, Z. Zeng, N. Y. Hu, and S. Han, "Electrostatically Driven Complex Coacervation and Amyloid Aggregation of Tau Are Independent Processes with Overlapping Conditions," *ACS Chem. Neurosci.*, Jan. 2020, doi: 10.1021/acschemneuro.9b00627.

[39] W. Kunz, J. Henle, and B. W. Ninham, "'Zur Lehre von der Wirkung der Salze' (About the science of the effect of salts): Franz Hofmeister's historical papers," *Curr. Opin. Colloid Interface Sci.*, vol. 9, no. 1–2, pp. 19–37, 2004, Accessed: Jul. 03, 2020. [Online]. Available: https://epub.uni-regensburg.de/24565/.

[40] Y. Zhang and P. S. Cremer, "Interactions between macromolecules and ions: the Hofmeister series," *Curr. Opin. Chem. Biol.*, vol. 10, no. 6, pp. 658–663, Dec. 2006, doi: 10.1016/j.cbpa.2006.09.020.

[41] R. A. Curtis, C. Steinbrecher, M. Heinemann, H. W. Blanch, and J. M. Prausnitz, "Hydrophobic forces between protein molecules in aqueous solutions of concentrated electrolyte," *Biophys. Chem.*, vol. 98, no. 3, pp. 249–265, Aug. 2002, doi: 10.1016/S0301-4622(02)00071-6.

[42] T. Ghosh, A. Kalra, and S. Garde, "On the Salt-Induced Stabilization of Pair and Many-body Hydrophobic Interactions," *J. Phys. Chem. B*, vol. 109, no. 1, pp. 642–651, Jan. 2005, doi: 10.1021/jp0475638.

[43] M. K. Braun *et al.*, "Reentrant Phase Behavior in Protein Solutions Induced by Multivalent Salts: Strong Effect of Anions Cl– Versus NO3–," *J. Phys. Chem. B*, vol. 122, no. 50, pp. 11978–11985, Dec. 2018, doi: 10.1021/acs.jpcb.8b10268.

[44] Y. Zhang and P. S. Cremer, "The inverse and direct Hofmeister series for lysozyme," *Proc. Natl. Acad. Sci.*, vol. 106, no. 36, pp. 15249–15253, Sep. 2009, doi: 10.1073/pnas.0907616106.

[45] G. Krainer *et al.*, "Reentrant liquid condensate phase of proteins is stabilized by hydrophobic and non-ionic interactions," *bioRxiv*, p. 2020.05.04.076299, May 2020, doi: 10.1101/2020.05.04.076299.

[46] S. H. Scheres, W. Zhang, B. Falcon, and M. Goedert, "Cryo-EM structures of tau filaments," *Curr. Opin. Struct. Biol.*, vol. 64, pp. 17–25, Oct. 2020, doi: 10.1016/j.sbi.2020.05.011.

[47] S. Kroschwald, S. Maharana, and A. Simon, "Hexanediol: a chemical probe to investigate the material properties of membrane-less compartments," *Matters*, vol. 3, no. 5, p. e201702000010, May 2017, doi: 10.19185/matters.201702000010.

[48] K. Ribbeck and D. Görlich, "The permeability barrier of nuclear pore complexes appears to operate via hydrophobic exclusion," *EMBO J.*, vol. 21, no. 11, pp. 2664–2671, Jun. 2002, doi: 10.1093/emboj/21.11.2664.

[49] S. S. Patel, B. J. Belmont, J. M. Sante, and M. F. Rexach, "Natively Unfolded Nucleoporins Gate Protein Diffusion across the Nuclear Pore Complex," *Cell*, vol. 129, no. 1, pp. 83–96, Apr. 2007, doi: 10.1016/j.cell.2007.01.044.

[50] A. D. Gitler, J. Shorter, T. Ha, and S. Myong, "Just Took a DNA Test, Turns Out 100% Not That Phase," *Mol. Cell*, vol. 78, no. 2, pp. 193–194, Apr. 2020, doi: 10.1016/j.molcel.2020.03.029.

[51] S. Ambadipudi, J. G. Reddy, J. Biernat, E. Mandelkow, and M. Zweckstetter, "Residue-specific identification of phase separation hot spots of Alzheimer's-related protein tau," *Chem. Sci.*, vol. 10, no. 26, pp. 6503–6507, Jul. 2019, doi: 10.1039/C9SC00531E.

[52] J. N. Israelachvili, *Intermolecular and Surface Forces*. Academic Press, 2011.

[53] J. S. D'Arrigo, "Screening of membrane surface charges by divalent cations: an atomic representation," *Am. J. Physiol.*, vol. 235, no. 3, pp. C109-117, Sep. 1978, doi: 10.1152/ajpcell.1978.235.3.C109.

[54] Y. Lin, D. S. W. Protter, M. K. Rosen, and R. Parker, "Formation and Maturation of Phase-Separated Liquid Droplets by RNA-Binding Proteins," *Mol. Cell*, vol. 60, no. 2, pp. 208–219, Oct. 2015, doi: 10.1016/j.molcel.2015.08.018.

[55] M. Kubánková *et al.*, "Probing supramolecular protein assembly using covalently attached fluorescent molecular rotors," *Biomaterials*, vol. 139, pp. 195–201, Sep. 2017, doi: 10.1016/j.biomaterials.2017.06.009.

[56] J. E. Chambers *et al.*, "An Optical Technique for Mapping Microviscosity Dynamics in Cellular Organelles," *ACS Nano*, vol. 12, no. 5, pp. 4398–4407, May 2018, doi: 10.1021/acsnano.8b00177.

[57] S.-C. Lee *et al.*, "Fluorescent Molecular Rotors for Viscosity Sensors," *Chem. – Eur. J.*, vol. 24, no. 52, pp. 13706–13718, Sep. 2018, doi: 10.1002/chem.201801389.

[58] M. K. Kuimova, G. Yahioglu, J. A. Levitt, and K. Suhling, "Molecular Rotor Measures Viscosity of Live Cells via Fluorescence Lifetime Imaging," *J. Am. Chem. Soc.*, vol. 130, no. 21, pp. 6672–6673, May 2008, doi: 10.1021/ja800570d.

[59] D. R. Robinson and W. P. Jencks, "The Effect of Concentrated Salt Solutions on the Activity Coefficient of Acetyltetraglycine Ethyl Ester," *J. Am. Chem. Soc.*, vol. 87, no. 11, pp. 2470–2479, Jun. 1965, doi: 10.1021/ja01089a029.

[60] A. Volkov, C. Dockter, T. Bund, H. Paulsen, and G. Jeschke, "Pulsed EPR determination of water accessibility to spin-labeled amino acid residues in LHCIIb," *Biophys. J.*, vol. 96, no. 3, pp. 1124–1141, Feb. 2009, doi: 10.1016/j.bpj.2008.09.047.

[61] J. M. Franck *et al.*, "Probing Water Density and Dynamics in the Chaperonin GroEL Cavity," *J. Am. Chem. Soc.*, vol. 136, no. 26, pp. 9396–9403, Jul. 2014, doi: 10.1021/ja503501x.

[62] A. Doll, E. Bordignon, B. Joseph, R. Tschaggelar, and G. Jeschke, "Liquid state DNP for water accessibility measurements on spin-labeled membrane proteins at physiological temperatures," *J. Magn. Reson. San Diego Calif 1997*, vol. 222, pp. 34–43, Sep. 2012, doi: 10.1016/j.jmr.2012.06.003.

[63] B. D. Armstrong and S. Han, "Overhauser Dynamic Nuclear Polarization To Study Local Water Dynamics," *J. Am. Chem. Soc.*, vol. 131, no. 13, pp. 4641–4647, Apr. 2009, doi: 10.1021/ja809259q.

[64] J. M. Franck, Y. Ding, K. Stone, P. Z. Qin, and S. Han, "Anomalously Rapid Hydration Water Diffusion Dynamics Near DNA Surfaces," *J. Am. Chem. Soc.*, vol. 137, no. 37, pp. 12013–12023, Sep. 2015, doi: 10.1021/jacs.5b05813.

[65] T. F. Segawa, M. Doppelbauer, L. Garbuio, A. Doll, Y. O. Polyhach, and G. Jeschke, "Water accessibility in a membrane-inserting peptide comparing Overhauser DNP and pulse EPR methods," *J. Chem. Phys.*, vol. 144, no. 19, p. 194201, May 2016, doi: 10.1063/1.4948988.

[66] W. L. Hubbell and C. Altenbach, "Investigation of structure and dynamics in membrane proteins using site-directed spin labeling," *Curr. Opin. Struct. Biol.*, vol. 4, no. 4, pp. 566–573, Jan. 1994, doi: 10.1016/S0959-440X(94)90219-4.

[67] D. E. Budil, S. Lee, S. Saxena, and J. H. Freed, "Nonlinear-Least-Squares Analysis of Slow-Motion EPR Spectra in One and Two Dimensions Using a Modified Levenberg–Marquardt Algorithm," *J. Magn. Reson. A*, vol. 120, no. 2, pp. 155–189, Jun. 1996, doi: 10.1006/jmra.1996.0113.

[68] J. S. Hwang, R. P. Mason, L. P. Hwang, and J. H. Freed, "Electron spin resonance studies of anisotropic rotational reorientation and slow tumbling in liquid and frozen media. III. Perdeuterated 2,2,6,6-tetramethyl-4-piperidone N-oxide and an analysis of fluctuating torques," *J. Phys. Chem.*, vol. 79, no. 5, pp. 489–511, Feb. 1975, doi: 10.1021/j100572a017.

[69] D. Chen *et al.*, "Tau local structure shields an amyloid-forming motif and controls aggregation propensity," *Nat. Commun.*, vol. 10, no. 1, pp. 1–14, Jun. 2019, doi: 10.1038/s41467-019-10355-1.

[70] G. C. Ruben, T. L. Ciardelli, I. Grundke-Iqbal, and K. Iqbal, "Alzheimer disease hyperphosphorylated tau aggregates hydrophobically," *Synapse*, vol. 27, no. 3, pp. 208–229, 1997, doi: 10.1002/(SICI)1098-2396(199711)27:3<208::AID-SYN7>3.0.CO;2-H.

[71] A. Pavlova, E. R. McCarney, D. W. Peterson, F. W. Dahlquist, J. Lew, and S. Han, "Site-specific dynamic nuclear polarization of hydration water as a generally applicable approach to monitor protein aggregation," *Phys. Chem. Chem. Phys. PCCP*, vol. 11, no. 31, pp. 6833–6839, Aug. 2009, doi: 10.1039/b906101k.

[72] D. W. Peterson, H. Zhou, F. W. Dahlquist, and J. Lew, "A soluble oligomer of tau associated with fiber formation analyzed by NMR," *Biochemistry*, vol. 47, no. 28, pp. 7393–7404, Jul. 2008, doi: 10.1021/bi702466a.

[73] S. C. Warren *et al.*, "Rapid Global Fitting of Large Fluorescence Lifetime Imaging Microscopy Datasets," *PLOS ONE*, vol. 8, no. 8, p. e70687, Aug. 2013, doi: 10.1371/journal.pone.0070687.

[74] A. Pavlova, C.-Y. Cheng, M. Kinnebrew, J. Lew, F. W. Dahlquist, and S. Han, "Protein structural and surface water rearrangement constitute major events in the earliest aggregation stages of tau," *Proc. Natl. Acad. Sci.*, vol. 113, no. 2, pp. E127–E136, 2016,

901   Accessed: Mar. 23, 2016. [Online]. Available:
902   http://www.pnas.org/content/113/2/E127.short.
903 [75] Y. Fichou *et al.*, "Tau-Cofactor Complexes as Building Blocks of Tau Fibrils," *Front.*
904   *Neurosci.*, vol. 13, 2019, doi: 10.3389/fnins.2019.01339.
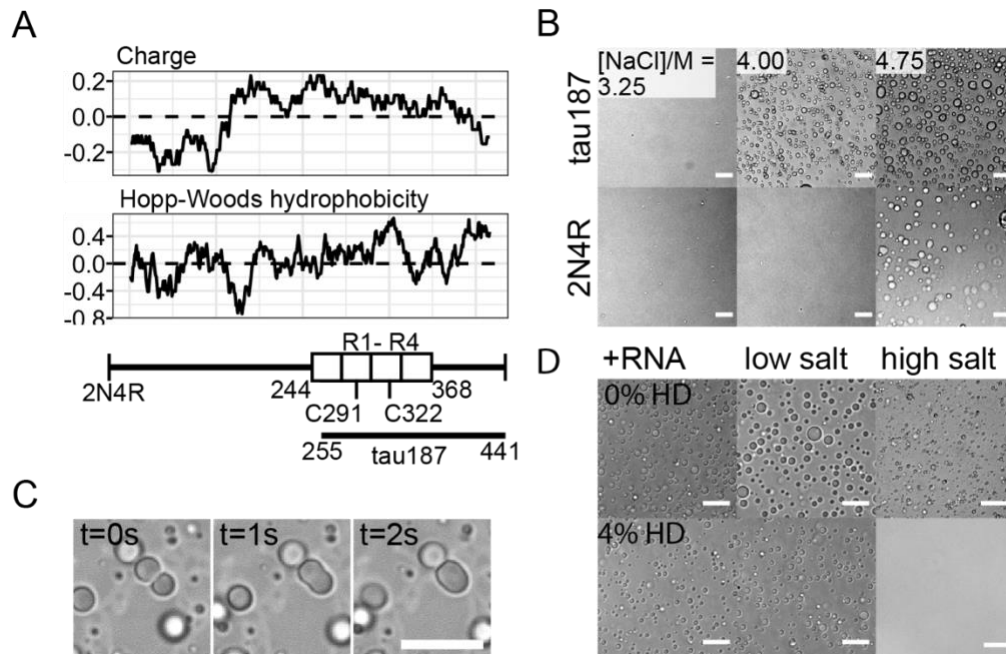905
906

Figure and Table Captions

908 **Figure 1**

909

910 **Figure 1 Tau undergoes LLPS at high salt concentration. A.** Charge and Hopp-Woods hydrophobicity plot of 2N4R. Data points show the average values of consecutive 25 amino acids. Reference values of Glycine are shown as dashed lines. tau187 fragment (residues 255-441), four repeat domains (R1–R4, 244-368) and two native cysteines (C291, C322) are shown. **B.** Microscope images of tau187 and 2N4R at varying [NaCl]. 44 µM tau187 and 20 µM 2N4R were chosen to have same mass concentration. Scale bar length is 25 µm. **C.** Droplet merging of tau LLPS-HS. 450 µM tau187 with 2.2 M NaCl was used. Scale bar length is 50 µm. **D.** Effects of 4 wt% 1,6-hexanediol on different types of tau LLPS. Tau-RNA LLPS (+RNA) was prepared with 20 µM 2N4R and 40 µg/mL polyU RNA; Tau low salt simple coacervation (low salt) was prepared with 20 µM 2N4R at 5 mM NaCl; Tau high salt simple coacervation (high salt) was prepared with 100 µM tau187 with 4.75 M NaCl. Scale bar length is 25 µm.

921

922 **Figure 1-figure supplement 1.**
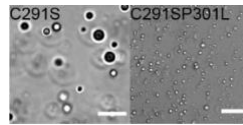
923

924

925 **Figure 1-figure supplement 1. Microscope images of LLPS-high salt of various tau constructs.**

926 450 µM Tau187C291S with 2.2 M NaCl; 100 µM tau187C291SP301L with 3.0 M NaCl.

927

928

929   **Figure 2**
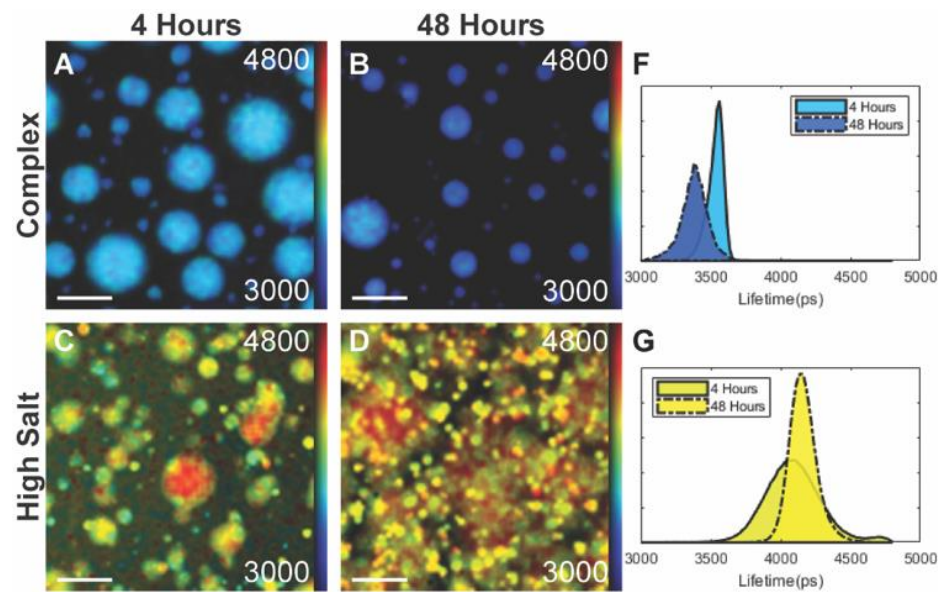
930
931   **Figure 2 FLIM fits of tau-RNA LLPS-CC (complex), and tau LLPS-high salt (high salt)**.
932   Fluorescence Lifetime Imaging Measurements were taken at 4 and 48 hours at the same resolution,
933   scale bar = 25 μm. **A-D,** Fluorescent microscope images of tau-RNA droplets and tau high salt
934   droplets before (4 hour) and after incubation (48 hour). Individual pixels were fitted with a 2-
935   component exponential decay using the FLIMfit software tool developed at Imperial College
936   London (Warren SC et al, PLOS ONE 2013), and the data were visualized using the higher lifetime
937   component. The colors in the fluorescent images and corresponding histograms represent a pseudo
938   color heat map that ranges from 3.0 to 4.8 ns, with blue representing low lifetimes and red
939   representing high lifetimes. **F-G.** Histograms of fitted results in A-D. The histograms are
940   normalized so that area under the curve is unity. The color under each histogram corresponds to
941   the pseudo color of the heat map at the histograms max value. Solid line = 4 hours, Dashed line =
942   48 hours.
943

944 **Figure 2-figure supplement 1.**

945
946
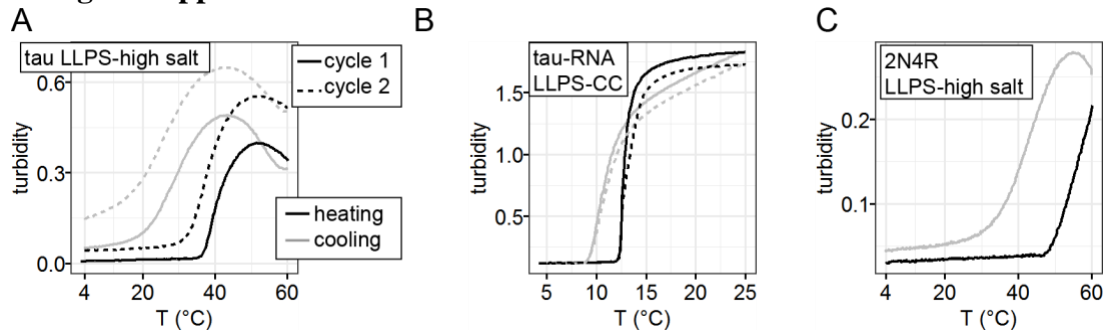
947 **Figure 2-figure supplement 1. Temperature dependence of LLPS-HS. A.** turbidity of tau187
948 LLPS-high salt upon heating-cooling cycles. 34 μM tau187 and 3.5M NaCl was used. **B.**
949 turbidity of tau187-RNA LLPS-CC upon heating-cooling cycles. 100 μM tau187 with 300
950 μg/mL PolyU RNA and 30 mM NaCl was used. **C.** turbidity of 2N4R LLPS-high salt upon
951 heating-cooling cycle. 20 μM tau with 3.5M NaCl was used. Samples were pre-cooled to 4 °C,
952 heated to 25 or 60 °C then cooled back to 4 °C (cycle 1, solid lines). A second cycle immediately
953 follows (cycle 2, dashed lines). The rate of both heating and cooling are 4 °C/min in A and C,
954 and 1 °C/min at B.

955

956 **Figure 2-figure supplement 2.**
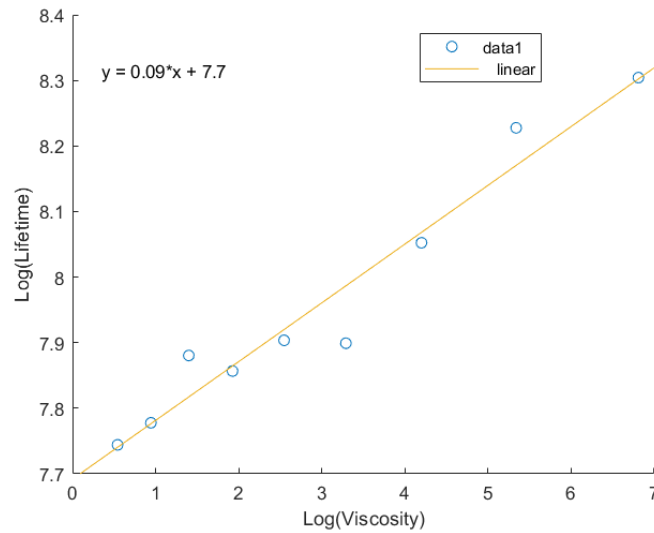
957
958 **Figure 2-figure supplement 2. Calibration and Fit of Fluorescent Lifetimes to a Glycerol**
959 **Standard Curve.** 4 µM 2N4R conjugated the BODIPY was placed in solutions of glycerol
960 concentrations in ddH$_2$O ranging from 20-100%. FLIM measurements of the solutions were
961 made and the resulting gaussians were fit and extracted in FLIMFit. The gaussians were fit and
962 the mean values were plotted on a log/log scale against the corresponding solutions viscosity.
963 The data was fit to the Förster Hoffman equation,

964
$$\log \tau = \log \frac{z}{k_0} + x \log \eta$$

965 Where τ is the lifetime in ps, $\log \frac{z}{k_0}$ is treated as a variable, x is the slope, and η is the viscosity in
966 centipoise. Fitting the data gave an equation of the form $y = 0.09x + 7.7$.

967

968   **Figure 2-figure supplement 3.**

969

970
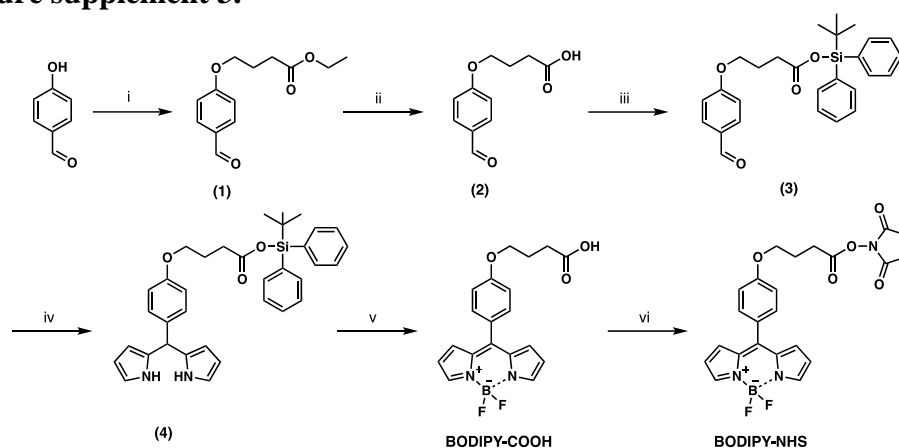
971   **Figure 2-figure supplement 3. Synthesis scheme of BODIPY-NHS**: (i) ethyl 4-bromobutyrate,
972   K_2CO_3, DMF, rt, 24 h, 98% yield; (ii) 2N KOH, MeOH, reflux, 2 h, 96% yield; (iii) DMAP,
973   Et_3N, THF then tert-butyl(chloro)diphenylsilane, 0°C to rt, 20 h, 68% yield; (iv) pyrrole, TFA, rt,
974   1 h, 66% yield. (v) DDQ, CH_2Cl_2, rt, 1 h and then $BF_3 \cdot (OEt_2)$, Et_3N, rt, overnight, 36% yield;
975   (vi) N-hydroxysuccinimide, DCC, DMAP, THF, 0°C to rt, overnight, 64% yield.
976

977 **Figure 3**

978

979
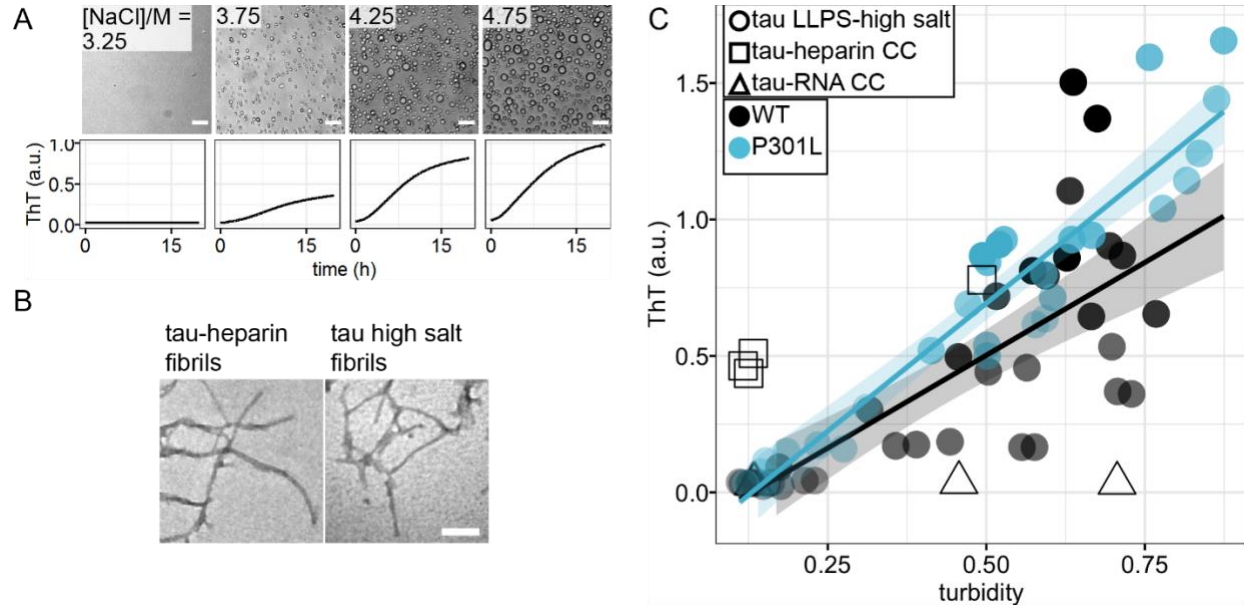
980 **Figure 3. Correlation of LLPS-high salt and amyloid aggregation. A.** Representative
981 microscope images at t = 0 and ThT fluorescence at room temperature overnight of tau LLPS-high
982 salt at various [NaCl]. 44 µM tau187 was used. **B.** Representative TEM image of tau LLPS-high
983 salt sample after overnight incubation, compared with tau-heparin fibrils. **C.** Correlation of initial
984 turbidity and final ThT fluorescence of tau LLPS-high salt vs LLPS-CC. Solids line and shadow
985 show linear regression and its standard error, respectively. 40 $\mu M \pm 10\%$ of tau187 was used.
986 Samples come from 5 different batches of proteins.

987

988 **Figure 3-figure supplement 1.**

989

990
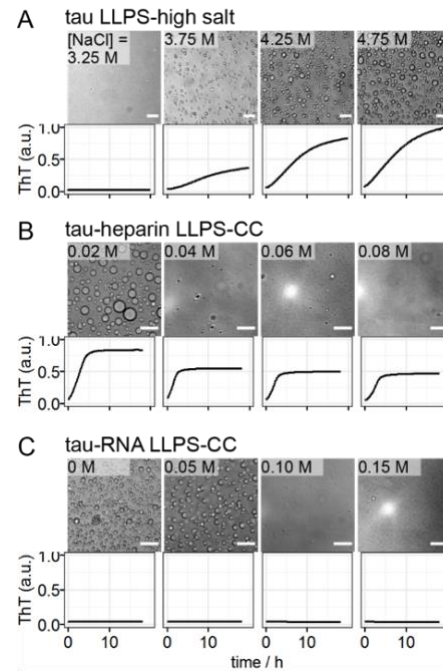
991 **Figure 3-figure supplement 1. Representative microscope images and ThT fluorescence at**

992 **room temperature overnight of tau LLPS-high salt, tau-heparin LLPS-CC, tau-RNA**

993 **LLPS-CC at various [NaCl].** 44 µM tau187, 73 µg/mL heparin and 132 µg/mL RNA were

994 used.

995

996   **Figure 3-figure supplement 2.**

997

998
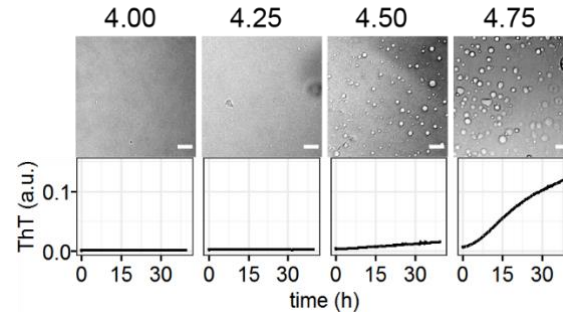
999   **Figure 3-figure supplement 2. Correlation of LLPS-high salt and amyloid aggregation of**
1000   **2N4R.** 20 μM 2N4R was incubated with varying [NaCl]. Microscope images were taken 10
1001   minutes after mixing while ThT fluorescence readings were recorded overnight. Scale bar length
1002   was 25 μm.

1003

1004 **Figure 3-figure supplement 3.**

1005
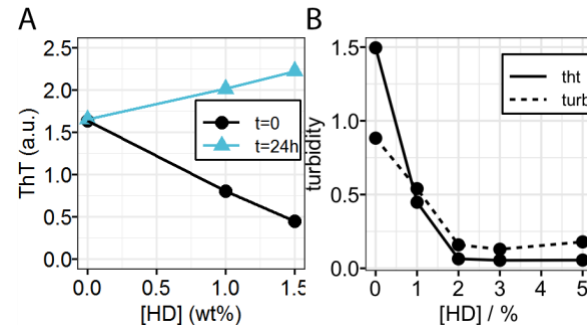
1006
1007 **Figure 3-figure supplement 3. Hexanediol dependence of ThT fluorescence and turbidity of**
1008 **LLPS-HS. A.** Varying concentration of 1,6-hexanediol were added to fresh LLPS-HS sample
1009 (t=0) and matured LLPS-HS sample (t=24h). After hexanediol was added, samples were
1010 incubated for 24 hours and ThT fluorescence was recorded. **B.** Initial turbidity and final ThT
1011 fluorescence of LLPS-HS samples mixed with varying concentration of 1,6-hexanediol. In both
1012 A and B, 100 µM tau187 and 3.0 M NaCl were used.

1013
1014

1015 **Figure 4**
1016
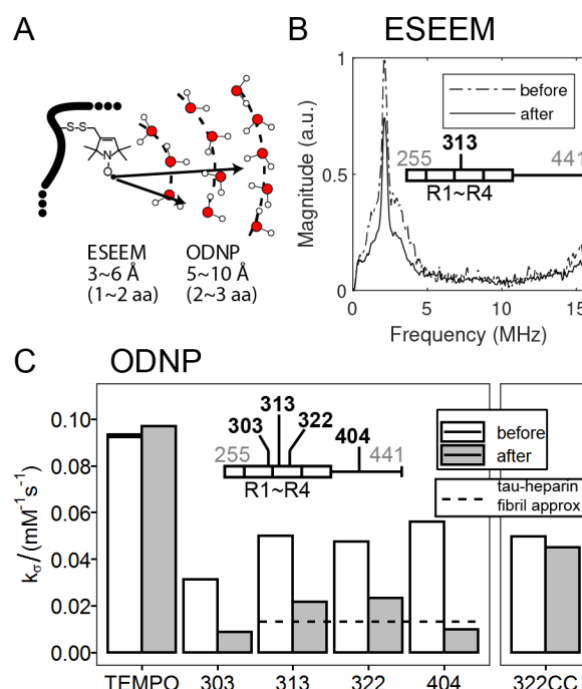
1017
1018
1019 **Figure 4 LLPS high salt undergoes dehydration. A.** Schematic diagram showing sensitive
1020 hydration shell in Electron Spin Echo Envelope Modulation (ESEEM) and Overhauser Nuclear
1021 Dynamic Polarization (ODNP). **B.** Representative 3 pulse-ESEEM of tau187 at site 313 at solution
1022 (before) and upon addition of 3.75 M NaCl (after). 22.5% Ficoll was used as glassing reagent. **C.**
1023 Representative ODNP cross-relaxivity parameter k_σ of tau187 at various sites at solution (before)
1024 and upon addition of 3.75 M NaCl (after). 250 µM tau was used. For comparison, k_σ of tau187 at
1025 site 322 upon tau-RNA complex coacervation was shown (322CC). 80% reduction of k_σ has been
1026 reported at site 313, 322 and 404 for tau-heparin fibrils (Pavlova, et al 2016), and is shown as
1027 dashed line.
1028

1029 **Figure 4-figure supplement 1.**

1030
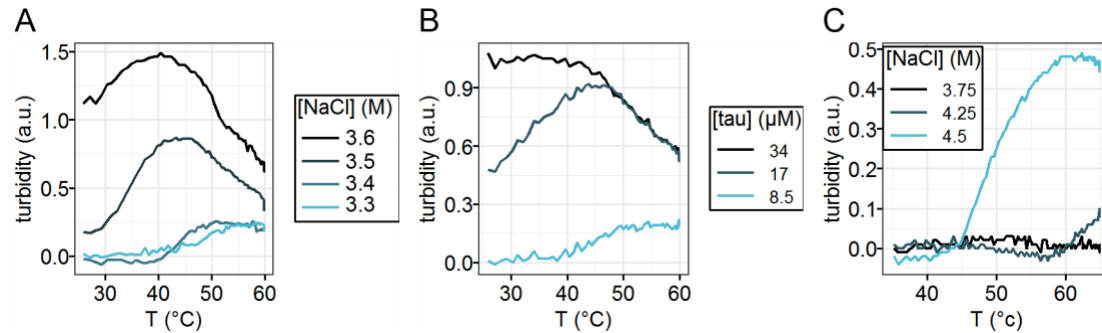
1031
1032 **Figure 4-figure supplement 1. LCST behavior of tau LLPS-high salt. A-B.** turbidity of
1033 tau187 LLPS-high salt upon heating at various [NaCl] with 34 μM tau (A) and at varying [tau]
1034 with 3.9 M NaCl (B). **C.** Turbidity of 2N4R (C291SC322S) LLPS-high salt upon heating and
1035 cooling at various [NaCl]. 20 μM tau was used. In A-C, samples were prepared at room
1036 temperature (25 °C) and heated to 65 °C at a rate of ~1°C/min.

1037
1038

1039 **Figure 4-figure supplement 2.**

1040
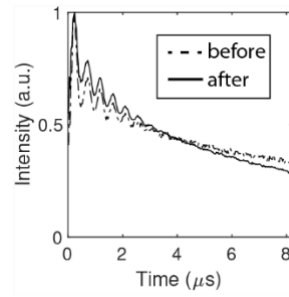
1041
1042
1043 **Figure 4-figure supplement 2. 3p-ESEEM data of tau187 upon LLPS-high salt in Figure**
1044 **5B.** Signals were scaled to 1 for comparison.
1045

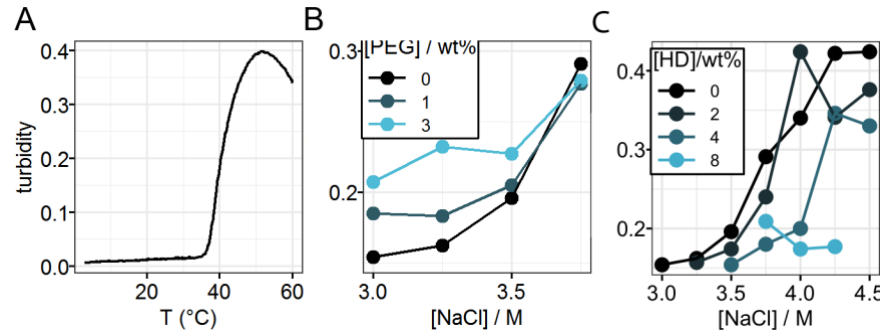1046 **Figure 4-figure supplement 3.**
1047

1048
1049 **Figure 4-figure supplement 3. Hydrophobic interaction drives tau LLPS-high salt. A**
1050 Turbidity of tau LLPS-high salt upon heating. 34 µM tau187 and 3.5 M NaCl was used.
1051 Samples were pre-cooled to 4 ℃ and heated up to 65 ℃ at a rate of 4 ℃/min. **B** Representative
1052 turbidity vs [NaCl] of tau LLPS-high salt at varying [PEG]. **C**. Turbidity of tau LLPS-high salt at
1053 varying [NaCl] and [HD]. In both B and C, 20 µM tau187 was used.
1054

Figure 4-source data 1.

site	k_σ / mM^{-1}S^{-1}	
	before	**after**
303	0.031	0.009
313	0.050	0.021
322	0.048	0.023
404	0.056	0.010
4OH-TEMPO	0.092	0.097
322CC	0.050	0.045

Figure 4-source data 1. ODNP measured k_σ in Figure 4.
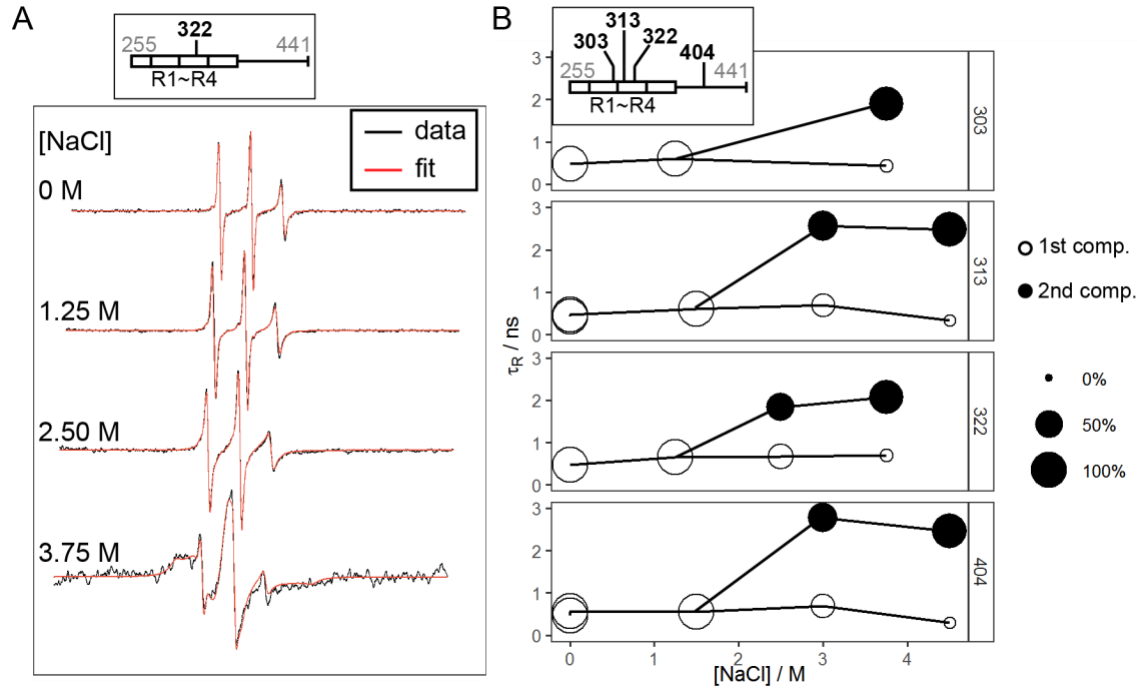
Figure 5

Figure 5. Site specific dynamics of tau187 upon LLPS-high salt. A. Representative X-band cwEPR lineshape of tau187 at site 322 at varying [NaCl]. Black lines show the experiment data and red lines show the fit. Spectra are shifted to avoid overlap. **B.** Rotational correlation time, τ_R, of tau187 at site 303, 313, 322 and 404 at varying [NaCl]. Data at low [NaCl] were fit with 1 component with the y-axis showing the τ_R. Data at high [NaCl] were fitted with 2 components with the area of the disk proportional to the percentage of each component.
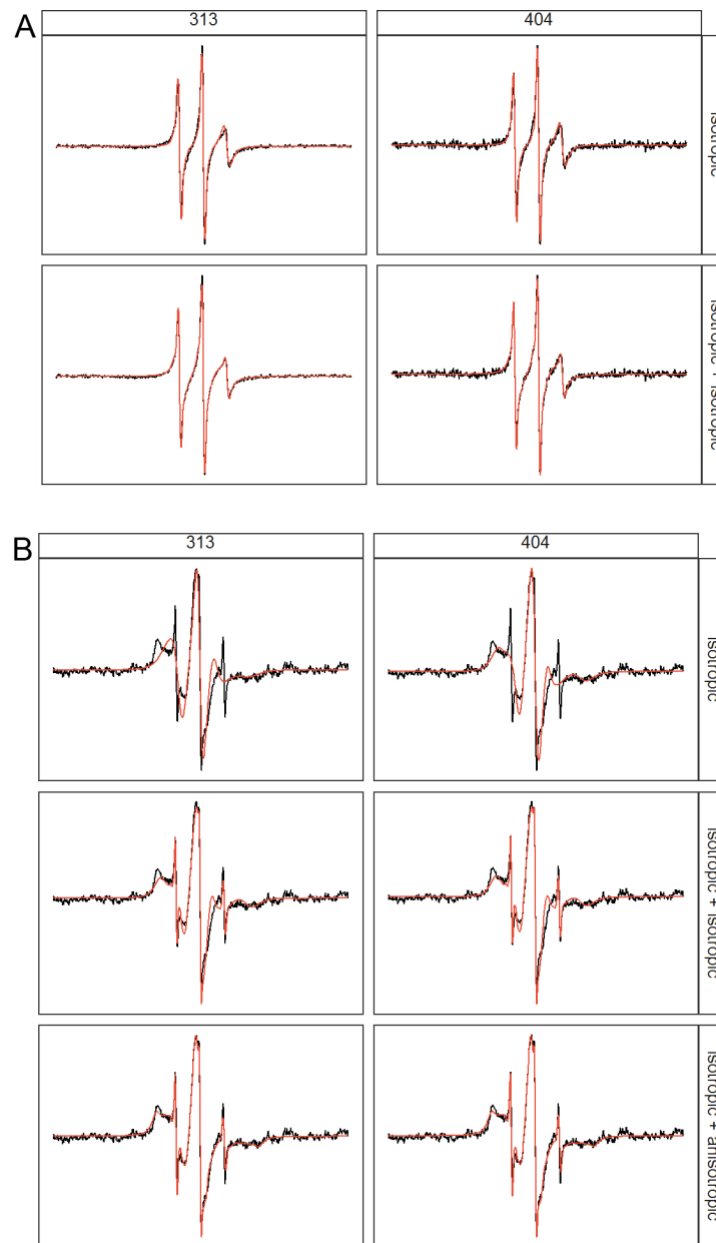
1071 **Figure 5-figure supplement 1.**

1072

1073

1074

1075 **Figure 5-figure supplement 1. Multicomponent and Anisotropic fitting of cwEPR**

1076 **lineshapes. A.** Comparison of 1 isotropic component fitting vs 2 isotropic component fitting of

1077 tau187 at site 313 and 404 at intermediate [NaCl] of 3.0 M. **B.** Comparison of 1 isotropic,

1078 isotropic+isotropic and isotropic+anisotropic components fit of tau187 at site 313 and 404 at

1079 very high [NaCl] of 4.5 M.

1080

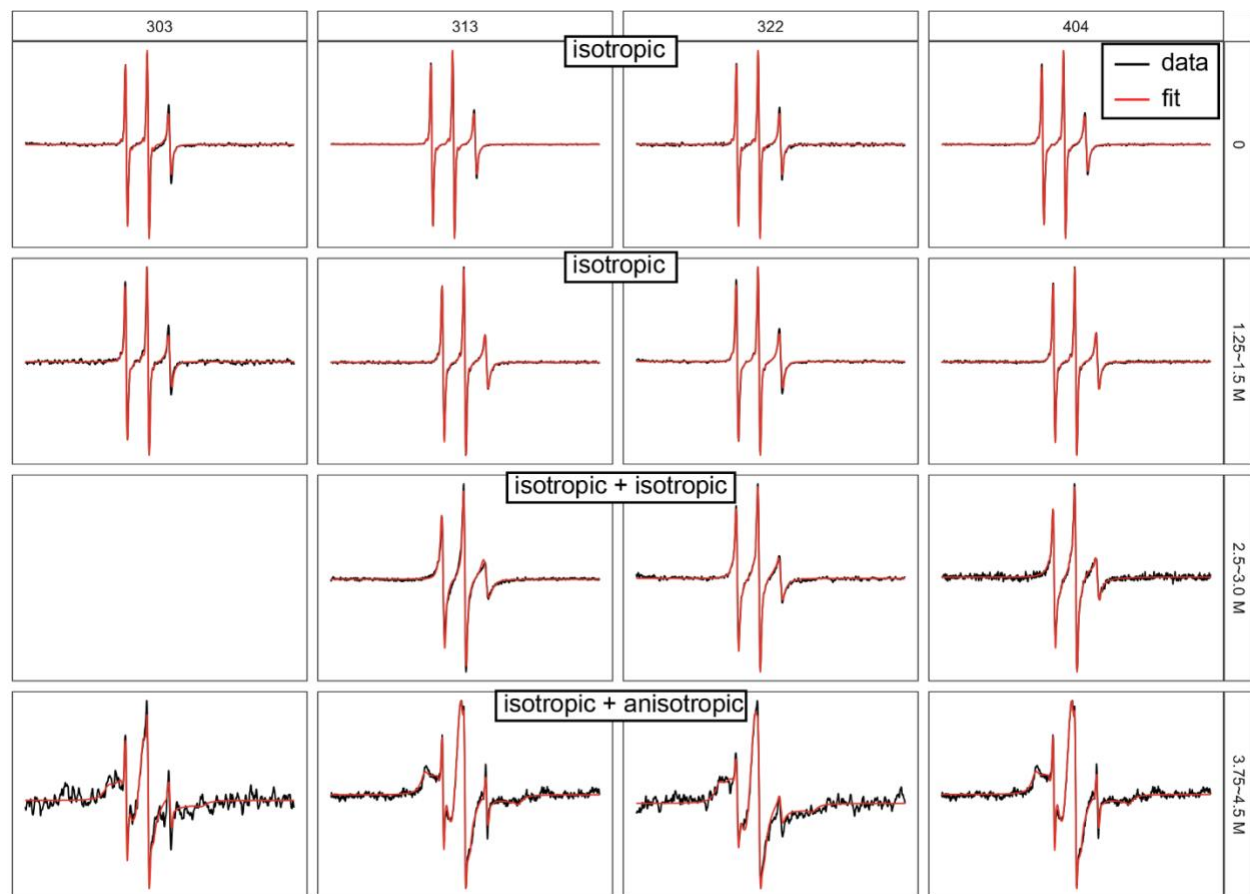1081 **Figure 5-figure supplement 2.**
1082

1083
1084
1085 **Figure 5-figure supplement 2. Best fit of cwEPR spectra of tau187 at varying sites and**
1086 **varying [NaCl].** Experiment details and fit results were shown in Figure 5B.
1087

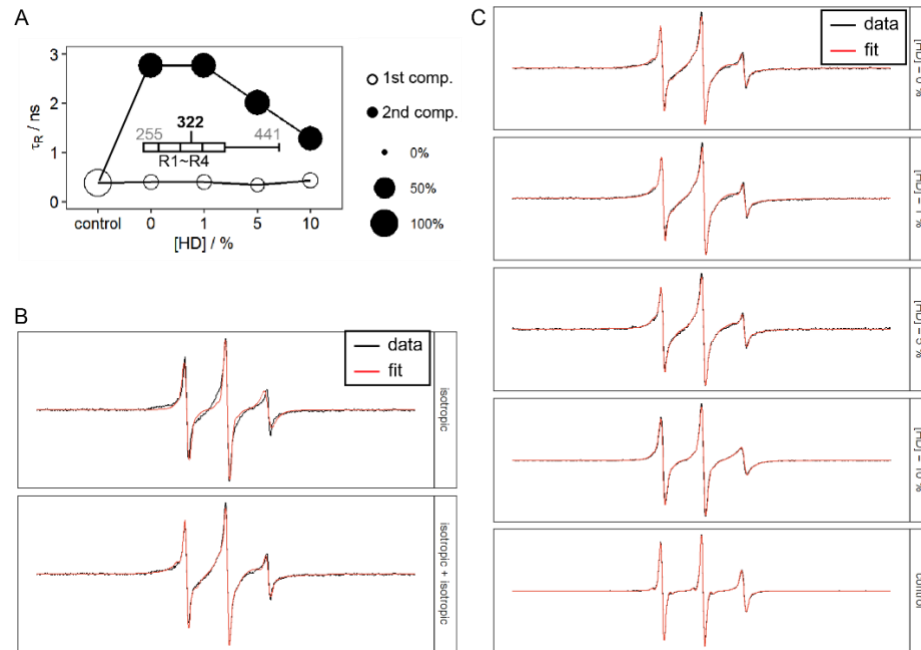**Figure 5-figure supplement 3.**

Figure 5-figure supplement 3. Effects of 1,6-hexanediol on tau LLPS-high salt. A. Rotational correlation time of tau LLPS-high salt at varying [HD]. 100 μM tau187P301LC322SL and 2.5 M NaCl were used. **B.** Comparison of fitting cwEPR lineshape using one component vs two component. [NaCl] = 2.5 M, [HD] = 0. **C.** cwEPR lineshape and fitting results of data in A.
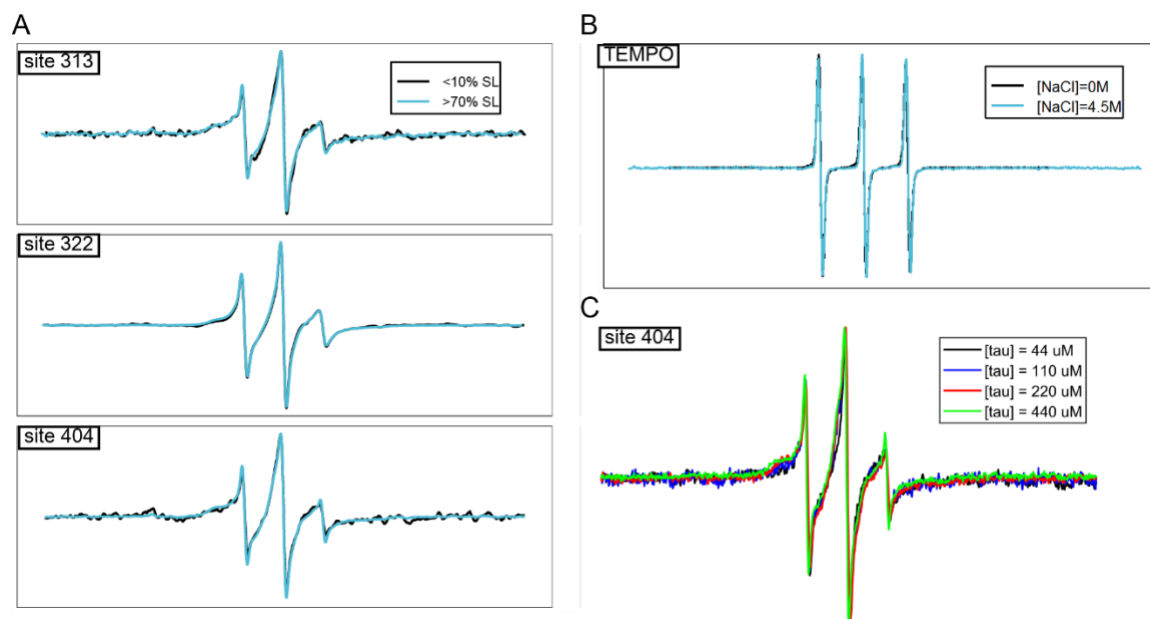
1097 **Figure 5-figure supplement 4.**
1098

1099
1100
1101 **Figure 5-figure supplement 4. Spin dilution and concentration dependence of cwEPR**
1102 **lineshape.** In order to gain information on the oligomer structure, we investigated the site-
1103 specific intermolecular interactions by cwEPR. Spin dilution, which consists in mixing 1 spin-
1104 labelled tau for 9 non-labeled tau, allows to diminish spin-spin dipolar coupling that could
1105 induce EPR lineshape broadening. By comparing cwEPR lineshape of spin-diluted sample vs
1106 non-spin-diluted sample, we can determine the population of spins that directly interact within a
1107 radius of ~1.5 nm. **A.** Effects of spin dilution on cwEPR lineshape of tau187 at site 313, 322 and
1108 404. 3.0 M NaCl was used. **B.** Effects of 4.5 M NaCl on 4OH-TEMPO cwEPR lineshape. **C.**
1109 Effects of concentrations on cwEPR lineshape of tau187 at site 404 at LLPS-HS conditions with
1110 3.0 M NaCl.

1111

1112 **Figure 5-source data 1.**

1113

site	[NaCl] / M	$t_{R,1}$ / ns	$t_{R,2}$ / ns	p_1 / %	p_2 / %
	0.00	0.48		100	
303	1.25	0.61		100	
	3.75	0.43	1.89	4	96
	0.00	0.42		100	
313	1.50	0.61		100	
	3.00	0.69	2.57	32	68
	4.50	0.34	2.48	3	97
	0.00	0.47		100	
322	1.25	0.65		100	
	2.50	0.68	1.83	40	60
	3.75	0.70	2.08	4	96
	0.00	0.47		100	
404	1.50	0.56		100	
	3.00	0.69	2.77	35	65
	4.50	0.29	2.45	3	97

1114

1115 **Figure 5-source data 1. Calculated parameters for cwEPR spectral simulation of tau187**
1116 **mutants 10 minutes after LLPS at various [NaCl].** Experiment details and fit results were
1117 shown in Figure 5B.
1118

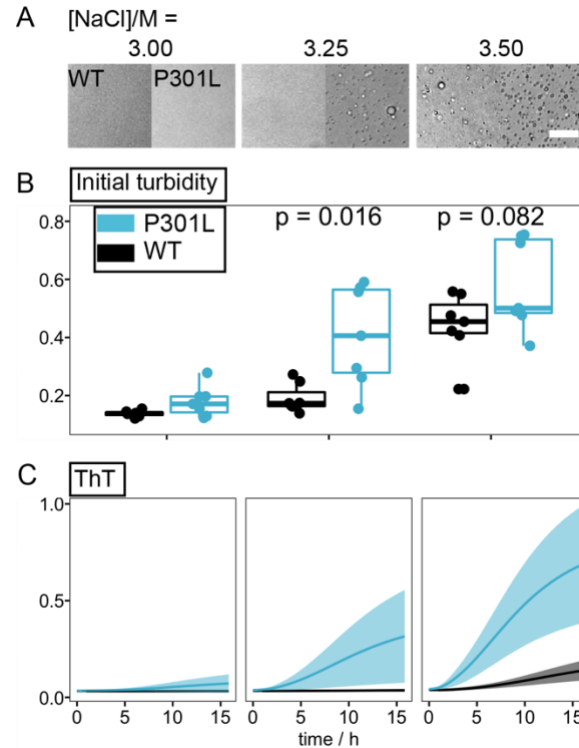1119 **Figure 6**
1120

1121
1122
1123 **Figure 6 Effects of P301L mutation on LLPS and amyloid aggregation of tau at high salt**
1124 **concentration. A.** Representative microscope images of tau187 Cysless and CyslessP301L
1125 mutants at varying [NaCl]. **B**. Turbidity of corresponding samples in A. **C**. ThT fluorescence of
1126 samples in A after overnight incubation at room temperature. ThT fluorescence was scaled by a
1127 constant of $2\times10_4$ throughout the manuscript. Ribbons in C show standard deviation of readings
1128 from 5 different batches of proteins.
1129

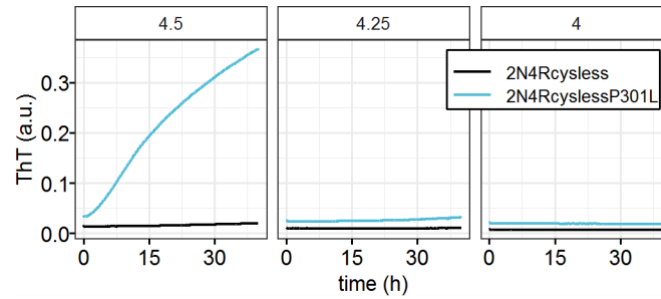1130 **Figure 6-figure supplement 1.**

1131

1132

1133 **Figure 6-figure supplement 1. Effects of P301L mutation on amyloid aggregation of 2N4R**
1134 **at high salt concentration.** 20 μM 2N4R was used. [NaCl] was shown in panel (unit: M).
1135 Samples were incubated at room temperature.
1136

1137 **Figure 6-figure supplement 2.**
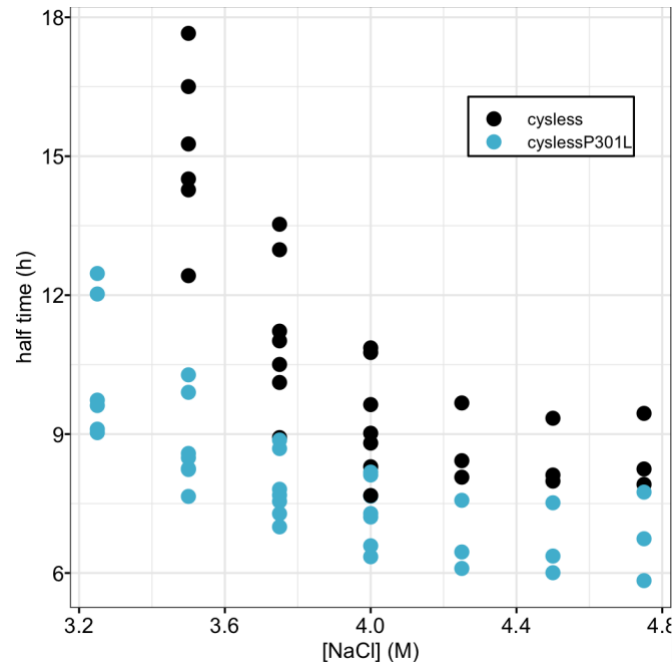
1138

1139
1140 **Figure 6-figure supplement 2. Effects of P301L mutation on half time of ThT fluorescence**
1141 **in high salt droplet conditions.** ThT fluorescence readings were recorded at varying [NaCl]
1142 using 34 µM tau187C291SC322S (cysless) and tau187C291SC322SP301L (cyslessP301L).
1143 Fluorescence readings were fit using a sigmoid function to extract the half time, defined as the
1144 time when ThT fluorescence reach half maximum. Data were obtained using n > 5 biological
1145 independent repeats.
1146